

Studies on TiO₂ Nanostructures
Synthesized by
Pulsed laser deposition and Electrochemical Anodization
Technique

A dissertation submitted in partial fulfillment of the Award of degree

MASTER OF SCIENCE

IN

PHYSICS

BY

Mr. Vijay Peddasingh (PH-2018-028)

Ms. Diksha K. Mishal (PH-2018-019)

Under the guidance of

Dr. RajeshKumar Shankar Hyam

UGC- Assistant Professor

Department of Physics

GOA UNIVERSTY

Taleigao Plateau – Goa

Certificate

This is to certify that the project entitled **Studies on TiO₂ Nanostructures Synthesized by Pulsed laser deposition and Electrochemical Techniques** is a bonafide work carried out by Vijay Peddasingh(PH-2018-028) And Diksha K. Mishal (PH-2018-019) Under the guidance of Dr. RajeshKumar Shankar Hyam As a part of curriculum for the degree in Master of Science In Physics during the academic year 2019-2020

Project Supervisor

(Dr. R. S. Hyam)

Head of the department

(Dr. K. R. Priolkar)

DECLARATION

We declare that this project has been completed by Mr.Vijay Peddasingh and Ms. Diksha K.Mishal and to the best of our knowledge, it has not been previously formed the basis for the award of any degree or diploma by any other university.

Vijay Peddasingh

PH-2018-028

Diksha K. Mishal

PH-2018-019

ANKNOWLEDGEMENT

It is our privilege and honor to express our deep gratitude and sincere thanks to Dr. Rajesh Kumar Shankar Hyam for his keen interest and unprecedented help in guiding us throughout this project work. We acknowledge our sincere thanks to Prof. Dr. Kaustub R. Priolkar, Head of the Department of Physics for rendering us the facilities for carrying out the work in Goa University. We are thankful to Mrs. Steffi Antony for constant support during experiments and characterizations. We also appreciate the help and support extended by the other faculty members, research scholars, non-teaching staff of the Physics Department and our friends. Last but not the least we express our deep gratitude to our families for their indispensable moral support.

Mr. Vijay Peddasingh

Ms. Diksha K. Mishal

Contents

CHAPTER 1 INTRODUCTION	1
1.1 Introduction	1
1.2 Physical properties	1
1.3 TiO ₂ phases and crystal structure	1
1.4 Applications of TiO ₂	2
1.5 Nano-materials	2
1.6 Aim and objective	3
CHAPTER 2 PULSED LASER DEPOSITION	4
2.1 Introduction	4
2.2 Apparatus	4
2.2.1 Laser Device	5
2.2.2 Ultra High Vacuum Chamber	5
2.2.3 Target and Substrate	7
2.3 Mechanisms of PLD process	8
2.3.1 Laser-target interaction	8
2.3.2 Plume expansion	10
2.3.3 Film Deposition	11
2.4 Laser Device	13
2.4.1 Functional Description of the Laser	13
2.4.2 Types of Lasers: Excimer Laser	17
2.4.3 Working principle of Excimer lasers	18
2.4.4 Design of Excimer laser	20
2.5 Vacuum System	23
2.5.1 Introduction	23
2.5.2 Vacuum Fundamentals	23
2.5.3 Generation of Vacuum	25
2.5.4 Vacuum measurement	29
CHAPTER 3 ELECTROCHEMICAL ANODIZATION OF TiO ₂	31
3.1 Introduction	31
3.2 Apparatus	32

3.3 Stages involved in TiO ₂ nanotube growth.....	32
3.4 Role of fluoride ions.....	35
3.5 Theoretical explanation for the stages involved in anodization process.....	36
3.6 Different stages involved in the Pore formation	37
3.7 Factors responsible for the change in geometry and composition	39
CHAPTER 4 CHARACTERIZATION TECHNIQUES.....	43
4.1 X-Ray Diffraction Technique.....	43
4.2 FTIR Spectroscopy.....	44
4.3 Scanning Electron Microscopy (SEM)	45
4.4 UV visible spectroscopy.....	46
CHAPTER 5 EXPERIMENTAL RESULTS AND DISCUSSIONS.....	49
5.1 Pulsed Laser Deposition.....	49
5.1.1 Introduction	49
5.1.2 Observations	49
5.1.3 Parameters	51
5.1.4 XRD.....	51
5.1.5 FTIR.....	53
5.1.6 SEM.....	54
5.1.7 Optical properties	56
5.2 Anodization	57
Conclusions	61
References	62

List of illustrations and Tables

Sr. No.	Object	Description
1.	Fig. 1.1	Common octahedral geometry of TiO ₂ with Ti atom at the centre, coordinated to 6 oxygen atoms and Different phases of crystalline TiO ₂ (rutile, brookite, anatase).
2.	Fig. 2.1	A schematic diagram of the Pulsed Laser Deposition system.
3.	Fig. 2.2	Ultra high vacuum chamber.
4.	Fig. 2.3	A) TiO ₂ pellets. B) The pellet is mounted on the stub which is attached carousel disc. C) Schematic diagram of the target carousel showing the motion of both target and the disc which is holding the target.
5.	Fig. 2.4	The three basic steps (processes) involved in the pulsed laser deposition.
6.	Fig. 2.5	A) A rectangular profile of an excimer laser. B) A rectangular groove formed on the pellet surface resulting from the ablation of target material by the interaction of excimer laser beam. C) An optical microscopic view of the groove. D) A SEM image of the cross-section of the groove.
7.	Fig. 2.6	A) A schematic diagram of the plume showing different regions of the plume. B) A blue colored plume inside the chamber during deposition process as visible from the gazing window.
8.	Fig. 2.7	A schematic diagram showing most common growth modes of film deposition.
9.	Fig. 2.8	Coherence excimer laser used in our PLD system.
10.	Fig. 2.9	Stimulated emission.
11.	Fig. 2.10	Schematic diagram showing the light amplification process in stimulated emission.
12.	Fig. 2.11	Schematic diagram of a typical laser device showing its three basic components.
13.	Fig. 2.12	Excimer laser transitions KrF laser.
14.	Fig. 2.13	A flow diagram of the simplified scheme of the KrF laser.
15.	Fig. 2.14	The interior view of the Coherence laser device. The main components of the device are: thyatron, service panel HV discharge unit and the laser

		tube.
16.	Fig. 2.15	A) A schematic diagram showing the primary components of the Coherence laser. B) Schematic diagram of the laser tube of the Coherence laser device.
17.	Fig. 2.16	Graph of pipe diameter, d versus pressure, P showing different flow regimes in the pipe with the variation of pressure of the gas.
18.	Fig. 2.17	A Hipace 300, turbo-molecular pump used in our UHV chamber. B) An oil-sealed rotary pump.
19.	Fig. 2.18	A schematic diagram of the typical vacuum system used in pulsed laser deposition.
20.	Fig. 2.19	Diagram showing the arrangement of the rotor and stator blades. B) The rotor blades of the turbo pumps down gas molecules out of the chamber.
21.	Fig. 2.20	When a gas molecule comes in contact with the rotor blade it gains velocity (or momentum).
22.	Fig. 2.21	A) A Pirani gauge for the measurement of low vacuum. B) A schematic diagram of the working principle of the Pirani gauge.
23.	Fig. 2.22	A) A schematic diagram of the Cold cathode gauge showing the internal components. B) A cold cathode gauge used for measuring high and ultra-high vacuum.
24.	Fig. 3.1	Anodization apparatus.
25.	Fig.3.2	A schematic diagram of oxide layer formation.
26.	Fig. 3.3	A schematic diagram of tubular growth structure.
27.	Fig.3.4	A general diagram showing field aided transport of mobile ions through the oxide layer in the absence and presence of fluoride ions.
28.	Fig. 3.5	A typical current-time curve after applying a voltage in the absence and presence of fluoride ions.
29.	Fig. 3.6	The three different stages involved in the formation of TiO_2 nanotube arrays (I-III).
30.	Fig. 3.7	Structure of a typical TiO_2 nanotube formed in organic electrolyte.
31.	Fig. 4.1	Schematic diagram of FTIR spectrometer.
32.	Fig. 4.2	Schematic diagram of UV spectrometer.

33.	Fig. 4.3	Bragg's law.
34.	Fig. 4.4	Schematic diagram of the scanning electron microscope.
35	Fig. 5.1	A) Variation of energy with charging voltage. B) Constant energy mode: voltage increases with time. C) Constant voltage mode: energy decreases with time.
36.	Fig. 5.2	XRD pattern of TiO ₂
37.	Fig. 5.3	XRD pattern of TiO ₂ thin films
38.	Fig. 5.4	FTIR spectrum of TiO ₂
39.	Fig. 5.5	A) Low density of Island aggregation which primarily depends on replate and laser fluence. B) High density of Island aggregation of the same sample showing uneven film deposition. C) A typical Island formation in PLD. D) Morphology of the air-annealed sample.
40.	Fig. 5.6	UV-Visible spectrum of as-deposited and air and vacuum annealed TiO ₂ films.
41.	Table 2.1	Lasing species for the excimer laser.
42.	Table 2.2	The accepted categories of the vacuum with the corresponding pressure ranges.
43.	Table 5.1	Observations table of the PLD parameters studied for the optimization.
44.	Table 5.2	Parameters of PLD.

CHAPTER 1

INTRODUCTION

1.1 Introduction

Titanium dioxide also called as titanium (IV) oxide is a naturally occurring oxide of titanium with a molecular formula TiO_2 . It is obtained from natural sources such as mined ilmenite ore and other minerals. Among all transition metal oxide, TiO_2 is the mostly studied compound due to its intrinsic properties. It has gained importance in both theoretical and experimental fields.

1.2 Physical properties

TiO_2 is an Odorless, insoluble compound with a Melting point $1,843\text{ }^\circ\text{C}$ and Boiling point $2,972\text{ }^\circ\text{C}$. Pure titanium dioxide is a fine white powder and widely used pigment because of its brightness. Its molecular weight is estimated to about 79.866 g/mol . TiO_2 is also an effective opacifier in powder form. Bulk TiO_2 is environmentally friendly, very useful and corrosion resistant material. It exhibits semiconducting properties which enables its use in solar cells and for photocatalytic reactions.

1.3 TiO_2 phases and crystal structure

Anatase, rutile, and brookite are three naturally occurring polymorphs of TiO_2 . Other forms such as baddeleyite and $\alpha\text{-PbO}_2$ -types of TiO_2 can be chemically synthesized because of their existing high-pressure phases.²

TiO_2 structures formed at room temperature are often found to be amorphous in nature. It can be converted to other phases such as anatase or rutile by an atmospheric thermal treatment under optimized conditions. All the three phases of TiO_2 (anatase, rutile, brookite) have a common octahedral geometry with titanium atom at the centre surrounded by six oxygen atoms but the arrangement of these octahedral structure is different for these three phases, creating a tetragonal structure for anatase and rutile and forming an orthorhombic structure for brookite¹ as shown in Fig. 1.1 .

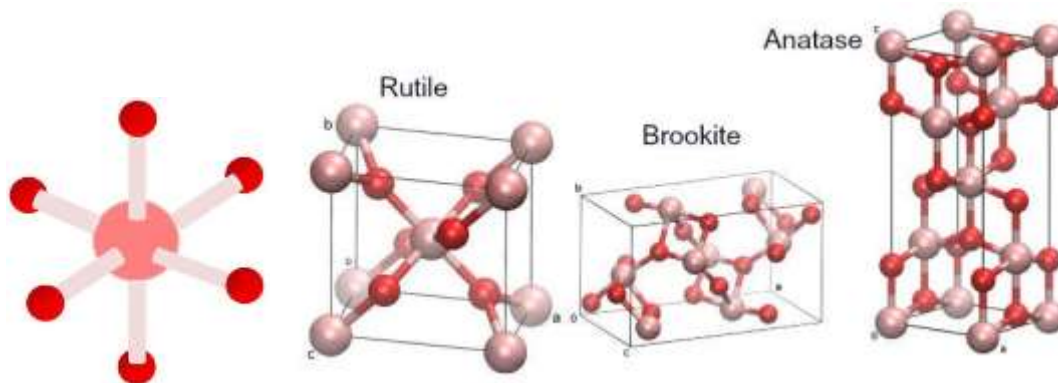


Fig. 1.1: Common octahedral geometry of TiO_2 with Ti atom at the centre, coordinated to 6 oxygen atoms and different phases of crystalline TiO_2 (rutile, brookite, anatase)¹.

Rutile is generally considered to be thermodynamically most stable at any temperature for larger particle size. Whereas, anatase and brookite phases are calculated to be thermodynamically stable at nanoscale level.

1.4 Applications of TiO_2

Titanium dioxide has a wide range of industrial and technological applications as pigment, photo catalyst and UV absorption. Hence, TiO_2 is an important compound suitable for fuel cells, solar cells, different sensors, pollution control system, waste management and self-cleaning glass coating materials along with food, cosmetics, paint and UV protector².

1.5 Nano-materials

Nanomaterials are basically small structures or small-sized materials and its dimension ranges from subnanometer to several hundred nanometers. Materials in nanometer scale exhibits different physical properties from that of bulk, which makes it distinctive from any higher order scales. In general, nanotechnology involves understanding the technology of design, fabrication and applications of nanomaterials. There are different approaches to fabricate and process nanostructures such as top-down and bottom-up approaches. In a top down synthesis method, the nanostructures are synthesized by breaking of materials to get nano-sized particles. Whereas, the growth of thin films is a bottom-up approach in which the nanostructures are synthesized onto the substrate by build-up of small size atoms, ion or molecules. However, the integration of top-down and bottom-up approaches are suitably best combination to produce order at nanoscale dimension and nanofabrication³.

1.6 Aim and objective

This dissertation addresses two major topics:

- 1) Physical technique: Pulsed laser deposition
 - i. To synthesize TiO_2 thin films on Soda lime glass substrate by pulsed laser deposition technique.
 - ii. Optimization of PLD chamber pressure.
 - iii. Optimization of substrate temperature by PID-controller.
 - iv. Optimization of laser parameters.
 - v. Qualitative study of thin films by using characterization techniques such as SEM, UV-visible spectroscopy, FTIR spectroscopy.
- 2) Chemical technique: Electrochemical anodization
 - i. To synthesize self-organised TiO_2 nanotube layer by electrochemical anodization optimized at low temperatures.
 - ii. To interpret the structure grown by controlled anodic oxidation of titanium metal substrate.
 - iii. To understand the basic mechanism of TiO_2 nanotubes grown in electrolyte incorporating fluoride ions.
 - iv. To study the factors affecting the geometry and composition of TiO_2 nanotubes.

CHAPTER 2

PULSED LASER DEPOSITION

2.1 Introduction

Pulsed Laser Deposition (PLD)^{4,6} is a physical vapor deposition technique which basically involves the use of high-energy laser to ablate the target material and deposit the ablated particles onto the substrate. It is a very flexible and advanced technique for the lab scale fabrication of nano-films. A generalized schematic representation of a PLD is shown in the Fig.2.1. The PLD system consists of an Ultra High Vacuum chamber, a High-Energy laser, a target and a substrate. The target and the substrate are located in the UHV chamber wherein they are positioned opposite to each other. The distance between them is adjusted in such a way to allow the ablated material to be deposited uniformly across the entire substrate.

The ablation and deposition processes are quite complex; there are so many factors which affect the quality of deposition. Different theoretical and empirical models^{7,8} have been developed to control the quality of thin film deposition. This chapter focuses on the basic mechanisms involved in the pulsed laser deposition of thin films and the parameters which affect their growth process.

2.2 Apparatus

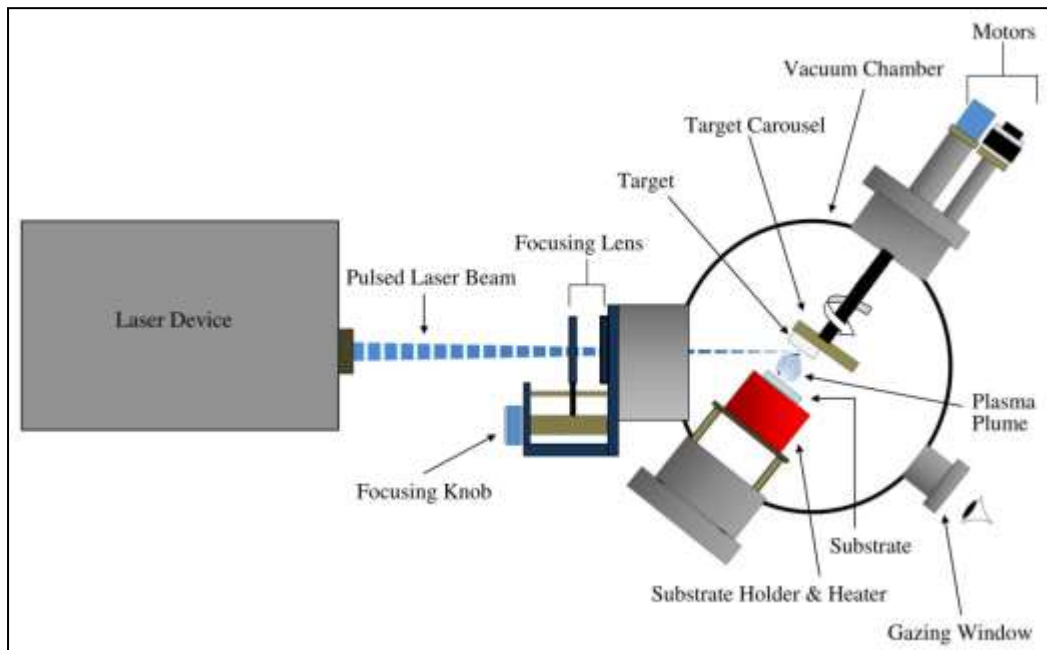


Fig. 2.1: A schematic diagram of the Pulsed Laser Deposition System.

2.2.1 Laser Device

The main component of PLD system is the laser device. The commonly used lasers in PLD systems are Excimer and Nd-YAG lasers. Excimer lasers are basically gas lasers; use of different gases gives different wavelengths. Typical excimer wavelengths are 157, 193, 248, 308, and 351 nm, which use gas fills of F₂, ArF, KrF, XeCl, and XeF, respectively. Depending on the wavelength of the laser (which is selectable by changing the excimer gas fill and the associated optics), the energy from the laser may either penetrate deeper into the target material, or get absorbed over a larger surface area of the target. This can lead to the ablation of large “chunks” of material in some cases; in other instances, part of the material may end up melting before it thermally evaporates. Neither of these scenarios is optimal and both should be avoided if the goal is to produce a high-quality film. Therefore, one must make a careful choice in balancing the target material, the laser wavelength, and the laser energy density.

Excimer laser operates in pulsed mode; laser pulse repetition rate⁹ plays an important role in the deposition process. There are two factors^{9,10} that determine an optimal laser pulse repetition rate: target heating from the laser energy, and allowing enough time for surface diffusion of the ablated species at proper lattice sites on the substrates. The latter becomes especially important to consider together with the temperature of the substrate, since surface diffusion is a thermal process that increases with increased temperature^{11,12}.

2.2.2 Ultra High Vacuum Chamber

The ultra-high vacuum chamber is a crucial part of PLD system which encloses the target and the substrate. Target is attached to the carousel mechanism which is controlled by the externally connected motors and the substrate is fixed onto the heating platform. The chamber is installed with all the necessary components for creating and controlling the vacuum. It is connected to the vacuum pumps which pump out the gas from the chamber. Vacuum gauges fixed to the chamber measure the vacuum. There are two valves to inlet the air into chamber in order to bring the chamber up to atmospheric pressure and there is also a main valve, called gate valve which isolates the chamber from the vacuum system whenever necessary. There is also a provision made for inletting the controlled flow of gas into the chamber for deposition in background gas environment. The gas flow is controlled by the mass flow controller. The details of the vacuum system and its operation is given in section 2.5

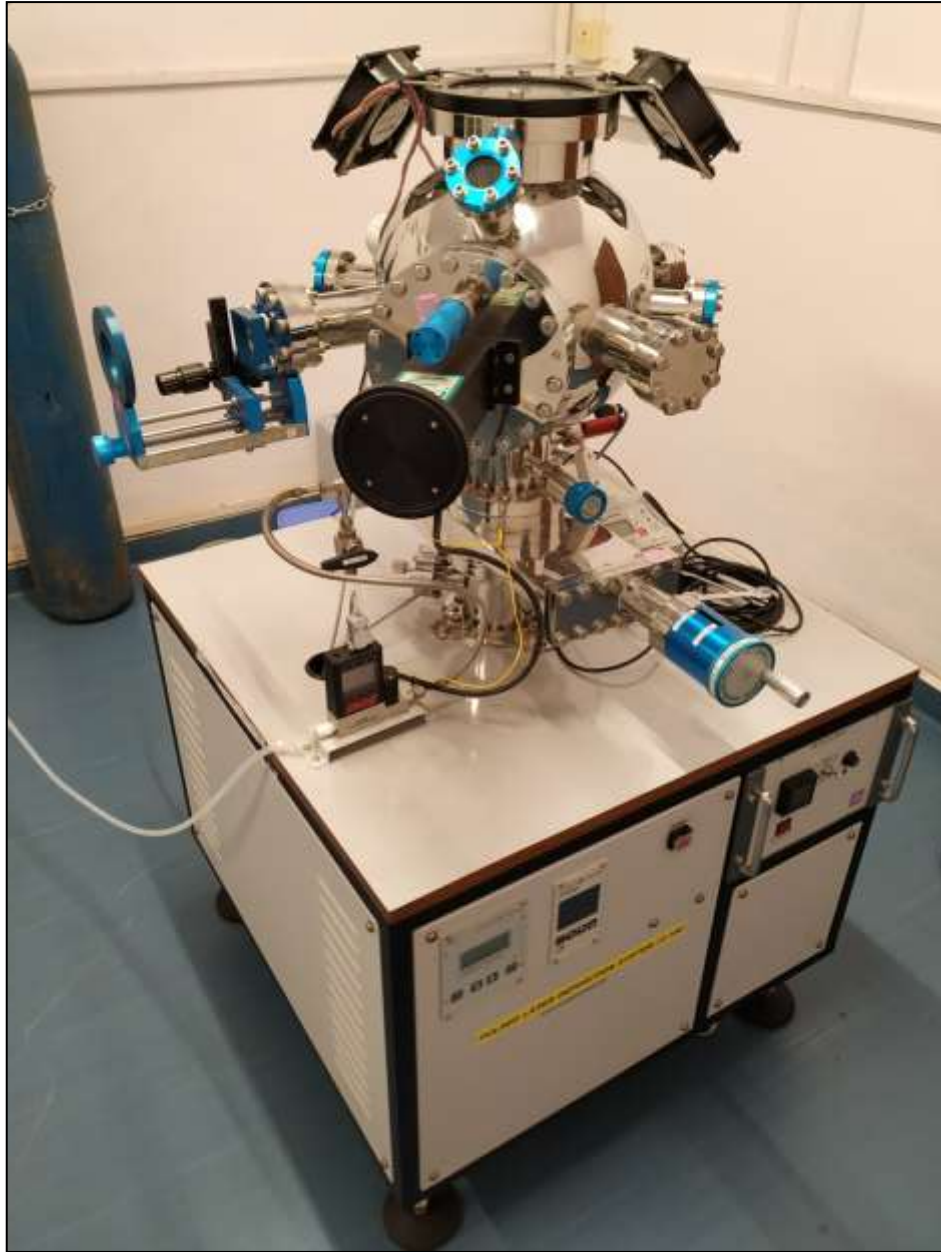


Fig. 2.2: *Ultra high vacuum chamber.*

2.2.3 Target and Substrate

The target material is usually made into pellet of desired dimension. In our system we have chosen TiO_2 as the target material and glass as the substrate. The pellet (Fig. 2.3A) is made out of commercially available TiO_2 (P25) powder; the required quantity of powder is mixed with acetone which acts a binder and grinded for two hours. The pellet is then sintered for one hour which evaporates the acetone.



Fig. 2.3: A) TiO_2 pellets. B) The pellet is mounted on the stub which is attached to carousel disc. C) Schematic diagram of the target carousel showing the motion of both target and the disc which is holding the target.

The pellet is mounted on the stub (Fig B) and the stub is connected to the carousel mechanism. The carousel mechanism helps the surface of the target to remain smooth and uniform during the entire deposition process. This, in turn, is one of the factors that help to ensure that the ablative plume remains constant. The combination of rotating the target and scanning (Fig. C) the laser across the diameter of the target allows the laser to cover the entire target surface uniformly with laser pulses, thus making the most efficient use of the target.

The substrate is fixed onto the heating platform whose heating process is regulated by a Proportional-Integral-Derivative (PID) controller device. Substrate heating is necessary because, the temperature of the substrate determines how quickly the deposited material diffuses across the surface of the substrate. This process allows the ablated species to incorporate at the proper lattice sites to create a smooth, crystalline film^{11,12}.

The distance between the target and the substrate is selected to match the deposition area with the size of a plasma plume to achieve uniform deposition across the entire substrate surface and also to avoid sputtering chunks of material onto the films. The size of the plume depends on the laser energy density^{6,10}, the background gas pressure, the target and even the wavelength of the laser.

2.3 Mechanisms of PLD process

The pulsed laser ablation is a very complex process but in simple terms it can be viewed as process wherein a pulsated laser beam is focused onto the surface of a target (solid or liquid)¹³ in a vacuum chamber and vaporizing the target material as a result of rapid boiling of the material within a localized interaction volume close to the surface of the target and ejected away from the target. This vapor is a collection of atoms, molecules, ions and electrons, the exact ratio and kinetic energy of which depend on the laser parameters (intensity, wavelength, pulse width) and to some degree on the target sample. The vapor drives towards the substrate and recondenses on its surface. The repeated pulses make more and more plume to be deposited on the substrate surface to form a thin film. The growth of this thin film takes different forms and depends on different parameters such as material flux, repetition rate, substrate material, substrate temperature, the target–substrate gap, chamber pressure, and background gas. The PLD process can be divided into the following steps: laser-target interaction, plume expansion and film deposition^{4,10}. These three steps are shown schematically in the Figure below.

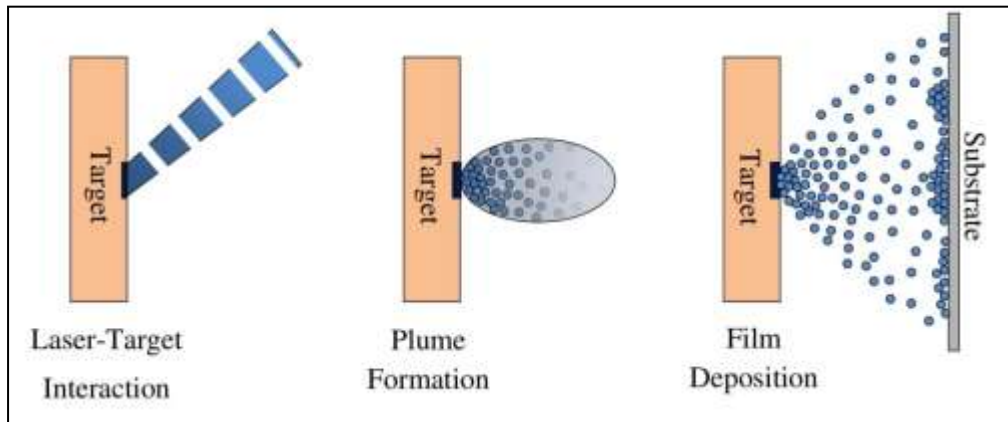


Fig. 2.4: The three basic steps (processes) involved in the pulsed laser deposition.⁴

2.3.1 Laser-target interaction

The laser-target interaction is generally divided into primary and secondary processes^{5,8,10}. The primary process is sub-divided into three more process—thermal, electronic and macroscopic sputtering and their relative dominance is dependent on the nature of target material, laser wavelength and pulse duration.

The electronic process initiates when a ultra-short laser pulse interacts with the target material and results in a very rapid excitation of the electron distribution, aided by an efficient electron–electron coupling leading to an immediate rise in the electron temperature, subsequent heating of the lattice at a rate dependent upon the electron–phonon coupling strength, and eventually vaporization of the transiently heated target.

When the longer laser pulses are used, thermal contributions generally dominate the process. This is because a sufficiently long duration allows the photon to couple with both electronic and vibrational modes the target material. Other favorable conditions for this process are low reflectivity, large absorption coefficient, low thermal diffusion and low boiling point.

In the macroscopic sputtering process the target material (macroscopic flakes) gets ejected and the amount of ejected flux changes dramatically when the laser fluence increases sufficiently to induce explosive boiling of the target material. This type of sputtering can arise when using target materials having high thermal expansion coefficients and a sufficiently high melting point. It can also arise in the case of porous targets, wherein the localised laser induced heating will cause very rapid expansion of any trapped gas pockets just below the surface and forcible ejection of the surface material. Fig. 2.5 B shows the ablated region of the target with an excimer laser which has a rectangular profile.

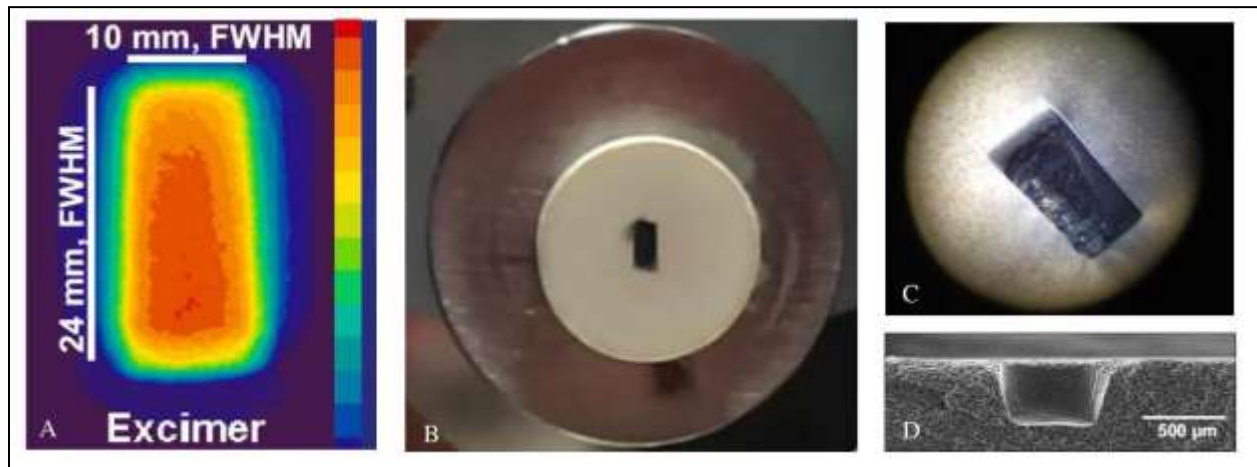


Fig. 2.5: A) A rectangular profile of an excimer laser¹⁴. B) A rectangular groove formed on the pellet surface resulting from the ablation of target material by the interaction of excimer laser beam. C) An optical microscopic view of the groove. D) A SEM image of the cross-section of the groove¹⁴.

Apart from the primary process, pulsed laser irradiation can lead to a number of indirect, or secondary, collision effects. The ejected particle will have some velocity and undergo collision-free expansion away from the interaction volume, if the density of the ablated material is sufficiently low. But in the early stages of the expansion, the density of the ablated material is high which results in rapid collisions between the particles. Due to these collisions, some fraction of the ablated material back-scattered towards the target surface; upon impacting the surface, these particles can induce secondary sputtering or recondense. This secondary sputtering can thus affect the ablation process especially when multi-target deposition is done. The secondary sputtering can be suppressed if the deposition is done in the presence of an appropriate background gas which constrains the higher density of ablated material in the early stages of plume expansion and enhanced probability of material re-deposition onto the target surface.

2.3.2 Plume Formation

This section attempts to briefly explain the formation, propagation and properties of the plasma plume typically encountered in PLD experiments, as revealed by numerous theoretical studies. The plasma plume resulting from the interaction of the nanosecond laser with the target surface expands away from the target surface; this process is independent of the primary ablation mechanisms and undergoes a series of changes which are termed as secondary ablation mechanisms; in the presence of background gas, these mechanisms will differ from those in the vacuum and in fact, the important growth parameters such as the spatial distribution, deposition rate, and kinetic energy distribution of the ablated species will also change. Here we only focus on plume expansion in vacuum.

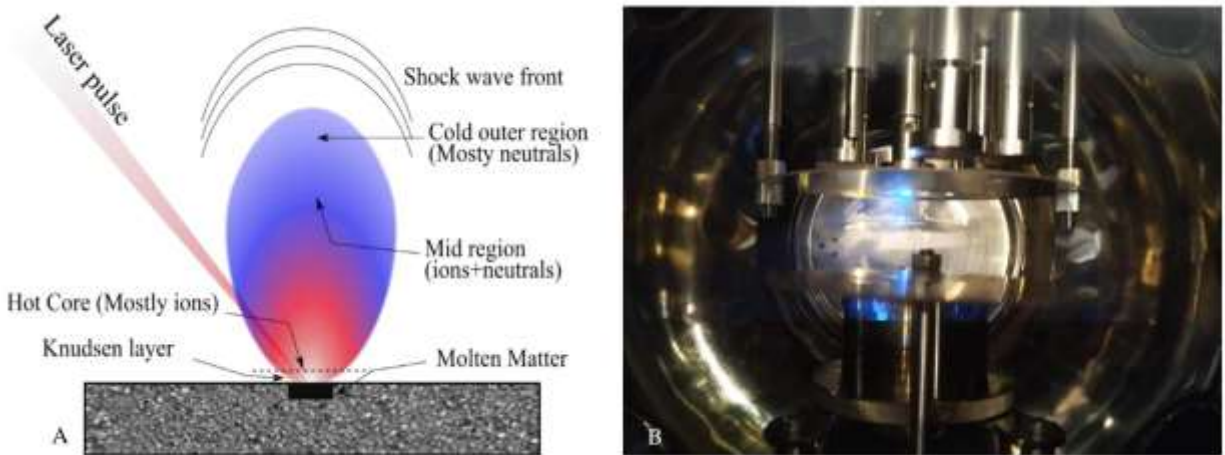


Fig. 2.6: A) A schematic diagram of the plume showing different regions of the plume²⁰. B) A blue colored plume inside the chamber during deposition process as visible from the gazing window.

Plume expansion in vacuum

During the laser-target interaction, the laser energy is absorbed by the localized volume of the target resulting in the ablation particles from that volume surface. These ablated particles which attain a temperature as high as 10000 K (which is well above the boiling point of most materials) form plasma in the region (close to the target surface), called Knudsen layer¹⁵. The density of the ablated particles in this region is high and all the particles in this region will have anisotropic velocity distribution with their velocity vectors pointing away from the surface. Later, this anisotropic distribution transforms into isotropic distribution by collisions among the ablated particles.

Soon after the laser-target interaction, i.e., when the laser pulse has terminated, the plasma plume tends to expand in the forward direction due to inter-particle collisions. The plasma is assumed to

have exponential density gradients, and the velocity of various species vary linearly from the center of the plasma. The acceleration and the expansion velocities in this regime are found to depend upon the initial velocities of the plasma. Consequently, the highest velocities are obtained in the direction perpendicular to the target surface, where the initial plasma dimension is only tens of micrometers.

The plume composition is complex¹⁰, and may change during expansion. In the first few millimeters of the plume expansion, emission from atoms and ions, multiple charged ions and possible molecules can typically be observed together with Bremsstrahlung emission in the plasma. Bremsstrahlung emission is basically the radiation given off by a charged particle (most often an electron) due to its acceleration caused by an electric field of another charged particle (most often a proton or an atomic nucleus). After the first few millimeters of expansion, Bremsstrahlung emission and emission from multiple charged ions are no longer observed. Typically, non-emitting particles (i.e. ground-state atoms and ions) have broader velocity distributions than emitting particles at PLD conditions²⁰.

2.3.3 Film Deposition

In ideal conditions the deposition of the ejected target material onto the substrate can be simply thought of as an adsorption of the ejected particles on the substrate surface but in the real environment this process is quite complex and depend on many factors such as substrate temperature, diffusional interactions within the film and with the substrate, etc, which modify the composition and properties of the growing film surface. In the following sections, we briefly discuss some of the typical film growth modes, growth characteristics and different film structures.

Typical growth modes

The ejected particles may interact with each other and nucleate before they come in contact with the substrate and diffuse on its surface. Considering this general theory of film nucleation and growth we may define the following three conventional modes of nucleation and growth which are named after their original investigators, Frank–van der Merwe, Volmer–Weber and Stranski–Krastanow:¹⁷⁻¹⁹

- a. The Volmer-Weber growth: Three-dimensional island growth
- b. The Frank-van der Merwe growth: Two-dimensional full-monolayer growth.
- c. The Stranski-Krastinov growth: Two-dimensional growth of full monolayers followed by nucleation and growth of three-dimensional islands

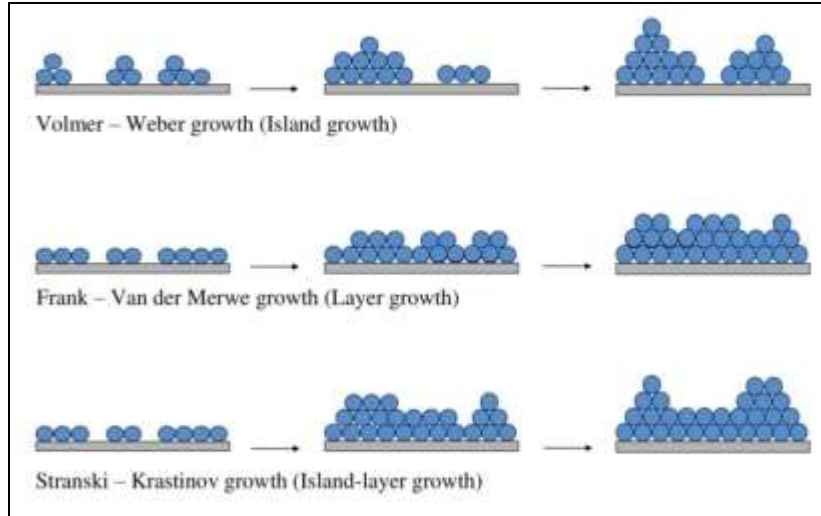


Fig 2.7: A schematic diagram showing most common growth modes of film deposition.¹⁷

(a) Volmer-Weber Nucleation and Growth

The atoms of the ablated material arrive at a rate dependent on the deposition parameters either on the bare substrate or on pre-deposited clusters of atoms and subsequently diffuse over the substrate or cluster surface. They may also encounter other ablated atoms to form mobile or stationary clusters or detach from them and re-evaporate. They could also directly land on the substrate surface and remain on it or re-evaporate from it. The balance between growth and dissolution processes for a given cluster will be governed by the total free energy of the cluster, ΔG , relative to an ensemble of individual atoms. For three-dimensional cluster growth, ΔG will have a maximum, ΔG^* , at a critical cluster size which means that cluster sizes above this critical size are stable.

(b) Frank - van der Merwe Nucleation and Growth

In this growth mode the nucleation and growth of islands is limited to monolayer thickness, i.e., a complete monolayer of atoms is formed on the substrate surface before significant clusters are developed on the next film layer. It is essentially a layer-layer by growth mode which has no free energy barrier to nucleation, i.e. no ΔG^* but depends on film-substrate bonding, film surface energy and substrate surface energy for its monolayer nucleation.

(c) Stranski-Krastinov Nucleation and Growth

This growth mode is similar to Frank-Van der Merwe growth initially but after 1-5 mono layers it may change to three-dimensional island growth. This might be the cause of an increase in stress with increasing layer thickness due to lattice mismatch.

2.4 Laser Device

In the previous sections we have seen how the laser plays central role in ablation process. In this section we will talk about it in a little more detail. We will look at the basic principle of the laser and then different types of lasers. Our PLD system uses a Coherence laser excimer laser (Fig. 2.8); we will also discuss about its basic working principle and construction in the following sections.



Fig. 2.8: *Coherence excimer laser used in our PLD system.*

2.4.1 Functional Description of the Laser

The term LASER is an acronym for Light Amplification by Stimulated Emission of Radiation; it has become so common and popular in everyday life that it is now referred to as laser. As the name suggests, stimulated emission is the basis for the working of laser. Stimulated emission is one of the three processes which happen when light interacts with matter. The first theoretical explanation of stimulated emission was given by Einstein in 1917 using Planck's law of radiation that was based on probability coefficients (also called Einstein coefficients) for absorption, spontaneous and stimulated emission of electromagnetic radiation. Theodore Maiman was the first to demonstrate the earliest practical laser in 1960 after the reports by several scientists²¹.

In this chapter, we solely discuss about the stimulated emission and how it is implemented in the laser device. Starting with the basic principles like, conditions for achieving stimulated emission, which are population inversion and pumping schemes then move on to explaining the basic design and working of the Excimer laser which is employed in our PLD system.

Stimulated Emission

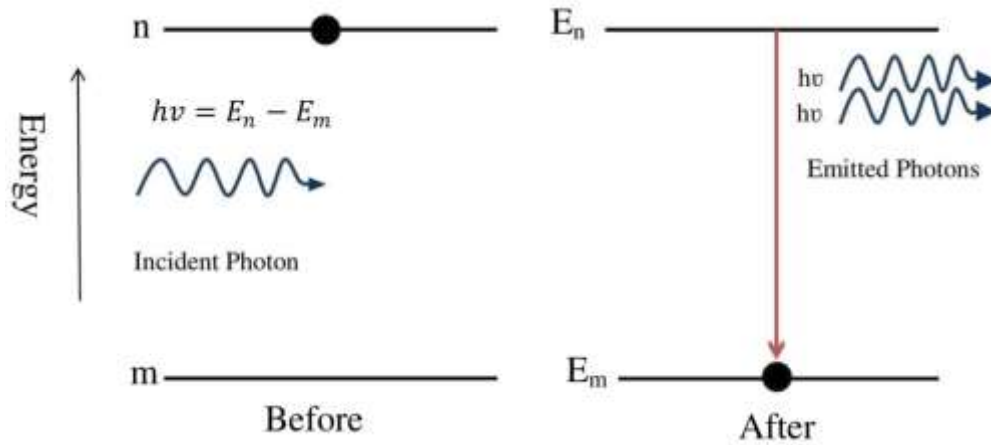


Fig. 2.9: Stimulated emission

According to Einstein, an atom in an excited energy state may, under the influence of the electromagnetic field of photon of frequency ν incident upon it, jump to a lower energy state, emitting an additional photon of same frequency ν . Thus, now two photons instead of one move on. This is known as stimulated emission of radiation (Fig. 2.9). The stimulated radiation is completely coherent with the stimulating radiation. As a result of this process, radiation passing through an assembly of atoms is amplified (Fig 2.10).

The probability of stimulated emission transition $n \rightarrow m$ is given by

$$P_{nm} = B_{nm} u(\nu)$$

where B_{nm} is the Einstein's coefficient of stimulated emission of radiation and $u(\nu)$ is the spectral energy density of incident radiation.

The total probability for an atom in state n to transit to the lower state m is therefore

$$P_{n \rightarrow m} = A_{nm} + B_{nm} u(\nu)$$

where, A_{nm} Einstein's coefficient of spontaneous emission of radiation.

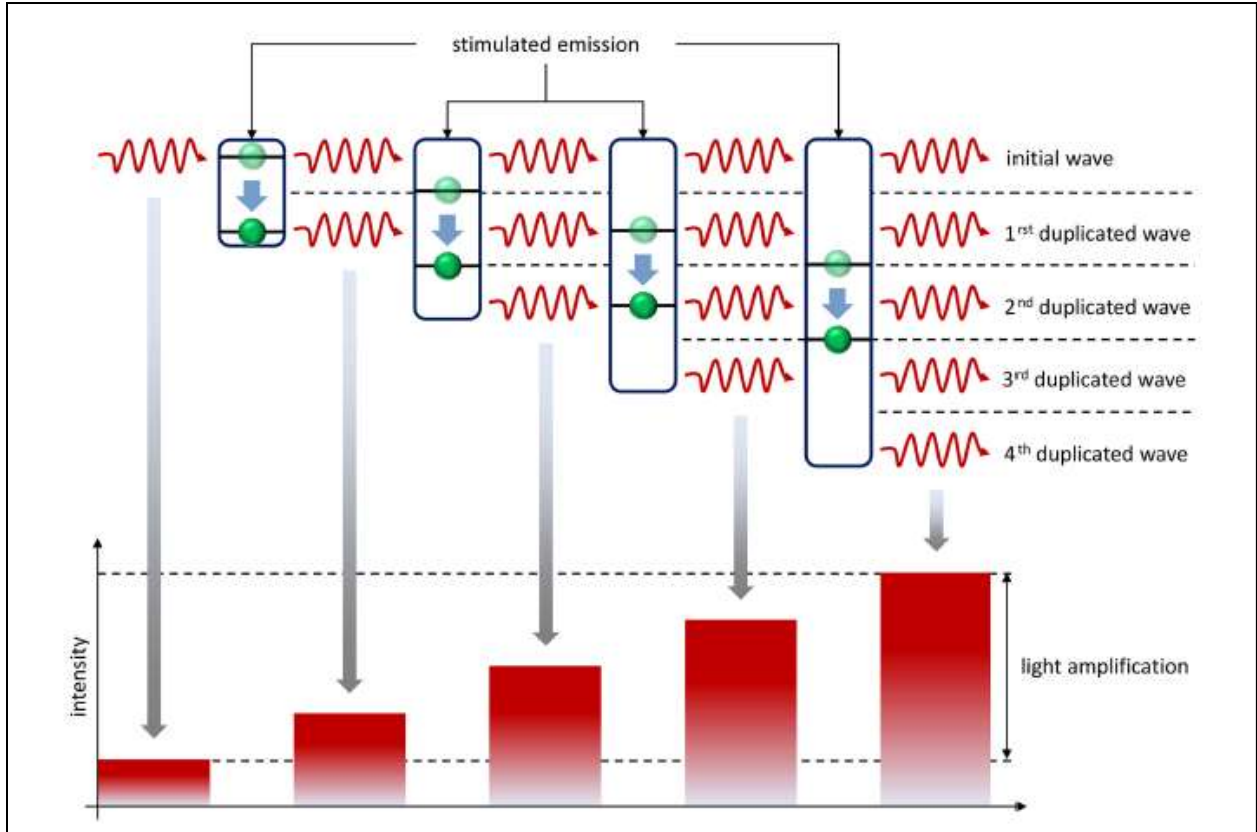


Fig. 2.10: Schematic diagram showing the light amplification process in stimulated emission²².

Population Inversion

At thermal equilibrium any material behaves as an absorber. So, considering an assembly of atoms in thermal equilibrium at temperature T with radiation of frequency ν and energy density $u(\nu)$, N_m and N_n being the number of atoms in states m and n respectively at any instant, the number of atoms in state m that absorb a photon and rise to state n per unit time is

$$N_m P_{m \rightarrow n} = N_m B_{mn} u(\nu)$$

Conversely, the number of atoms in the state n drops to m , either spontaneously or under stimulation, emitting a photon per unit time is

$$N_n P_{n \rightarrow m} = N [A_{nm} + B_{mn} u(\nu)]$$

For equilibrium,

$$N_m P_{m \rightarrow n} = N_n P_{n \rightarrow m}$$

Then, the distribution of populations in N_1 and N_2 of the ground state (levels 1) and the excited state (level 2) with energies E_1 and E_2 respectively, at thermal equilibrium is described by the Boltzmann statistics

$$\frac{N_m}{N_n} = e^{-\frac{(E_n - E_m)}{k_B T}}$$

where, k_B is the Boltzmann constant and T is the absolute temperature. At room temperature, $N_m > N_n$ and absorption will dominant over stimulated emission, if however, by some means a large number of atoms are made available in the higher energy state, i.e., $N_n > N_m$, stimulated emission is promoted. The situation in which the number of atoms in the higher state exceeds that in the lower state is known as population inversion. The process of achieving population inversion is known as pumping of atoms. When the pumping process is employed in optical region, it is called optical pumping otherwise it is either electrical or chemical pumping^{21,23}.

Laser construction

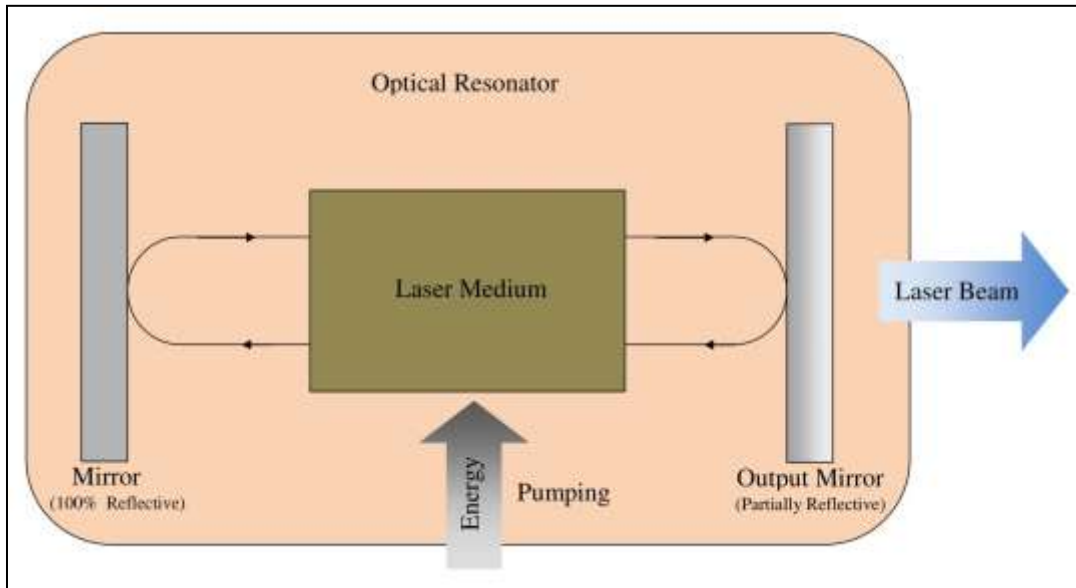


Fig.2.11: Schematic diagram of a typical laser device showing its three basic components.

Three basic components are needed for the laser construction:

- An active laser medium capable for emission of laser light.
- An optical resonator for the amplification of the laser light.
- And an energy source to stimulate the emission of the laser light.

An active laser medium can be a solid, a liquid or gaseous material. The atoms in this-laser active medium are pumped, or energized, to an excited state by an energy source. These atoms

are stimulated by external photons to emit (stimulated emission) the energy in the form of photons. The photons thus emitted travel in step with the stimulating photons and, in turn, impinge on other excited atoms to release more photons.

The emitted photons are further amplified by the optical resonator which normally consists of two mirrors which are placed on two sides of the active laser medium. Light amplification is achieved as the photons move back and forth between the two mirrors (one is fully reflective and the other is partially reflective), triggering further stimulated emissions. A part of the intense, directional, and monochromatic laser light finally leaves the resonator through one of the partially reflective mirror.

The energy source used in the laser device principally depends on the active lasing medium, and this also determines how the energy is transmitted to the medium. An Nd:YAG laser uses a light source from a Xenon flash lamp, Helium-Neon laser uses an electric discharge and the Excimer laser uses both an electric discharge and chemical reaction. The supply of energy to excite the gain medium to produce population inversion is called pumping; depending on the energy source this is called optical pumping, electrical pumping and chemical pumping.

2.4.2 Types of Lasers: Excimer Laser

The classification of lasers can be made by considering different aspects. Commonly the 'laser medium' is used as the basis for this classification. We therefore have: Gas lasers, Solid-state lasers, Semiconductor lasers, Liquid lasers, and some laboratory developments like free-electron lasers or X-ray lasers.^{24,25}

Gas lasers dominate any list of commercially available laser types and can emit radiation with the widest variety of wavelengths compared to lasers using other active media. Among them, excimer lasers are the most powerful lasers which exclusively emit laser irradiation in the ultraviolet wavelength range from 126 to 351 nm. Its active laser medium consists of so-called excimers; the name excimer comes from excited dimer, a class of molecules formed by the combination two identical constituents in the excited state. For the most common excimer lasers of today, the name "excimer" laser is used only by convention since here excited complexes (exciplexes) of rare-gas monohalides rather than excited dimers form the active laser medium is used. In addition, exciplexes exist with some stability only in the excited state. The rare-gas halide exciplexes are formed between the rare gasses Ar, Kr, or Xe and the halides F or Cl. The most important lasing species for the excimer laser are given in the table.

Sr. No.	Gas/gas mixture	Symbol/ molecular formula	Laser wavelength (nm)
1.	Argon	Ar_2	126
2.	Fluorine	F_2	157
3.	Xenon	Xe_2	172
4.	Argon fluoride	ArF	193
5.	Krypton chloride	KrCl	222
6.	Krypton fluoride	KrF	248
7.	Xenon bromide	XeBr	262
8.	Xenon chloride	XeCl	308
9.	Xenon fluoride	XeF	351

Table 2.1: *Lasng species for the excimer laser.*

2.4.3 Working principle of Excimer lasers

Considering the KrF as the active laser medium, the general principle of the excimer laser transitions is shown in the Fig. 1.12. The upper laser level is an ionically bound charge transfer state of the 2P rare-gas positive ion (Kr^+) and the 1S halogen negative (F^-). The upper laser level is formed by the electrically excited noble gas halide bond and laser irradiation is emitted during the transition to the non-excited noble gas halide bond, i.e. the lower laser level, where the emitted laser wavelength results from the potential difference of both levels. Although this process seems very simple, it actually relies on complex plasma reaction processes. As an example, a simplified reaction scheme for KrF is shown in Fig. 1.13^{26, 27, 28}.

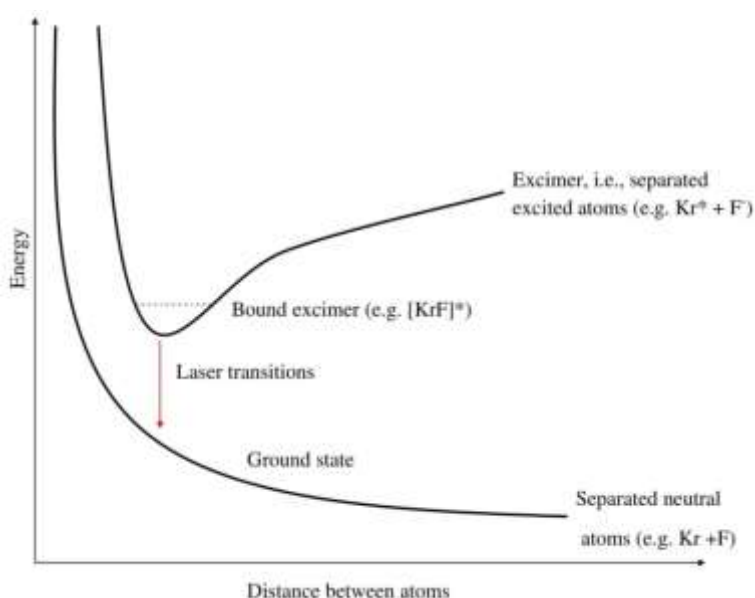


Fig. 2.12: Excimer laser transitions in KrF laser²⁷.

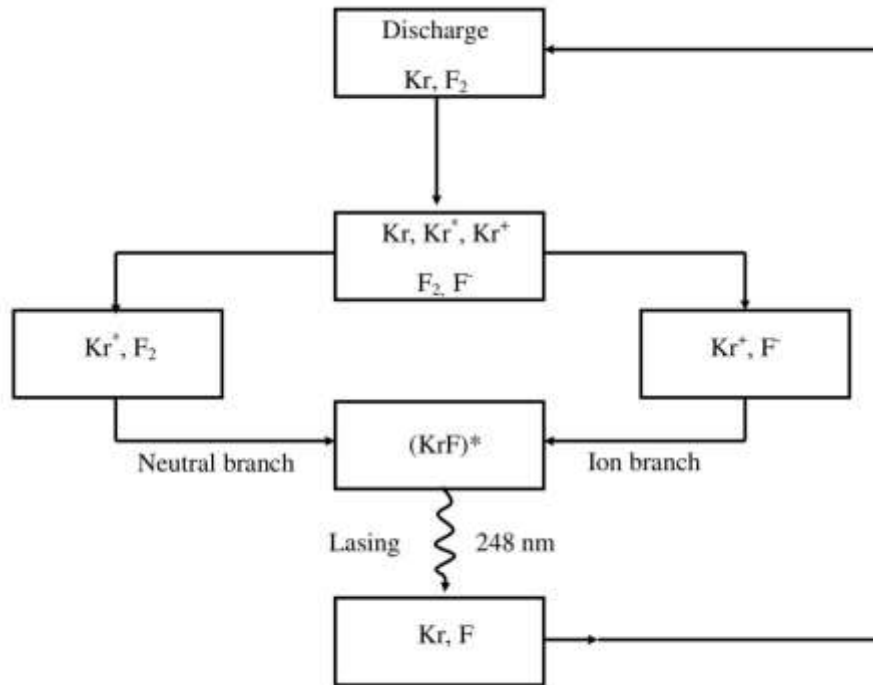


Fig. 2.13: A flow diagram of the simplified scheme of the KrF laser²⁸.

According to this scheme, the formation of the rare-gas halogen molecule is dominated by two reaction channels: The ion channel, where ion pair recombination of a positive rare-gas ion and a negative halide ion takes place in the presence of a third body (buffer gas, for example Ne or He), and by the neutral channel, where an excited-state rare-gas atom reacts with a halogen molecule in the so-called “harpooning reaction²⁹” which is basically a chemical reaction between two substances: one prone to form a cation and the other prone to form an anion.

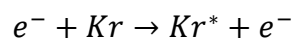
The most important expressions describing the inherent chemical reactions, the pumping and stimulated emission are shown below for the example of a KrF excimer laser.

Pumping:

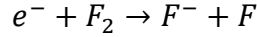
Positive inert-gas ion production,



Inert-gas metastable production,



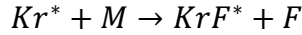
Negative halogen ion production,



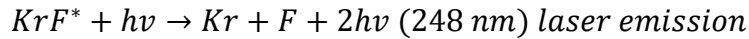
KrF^* production (ion branch),



KrF^* production (neutral branch),



Stimulated emission:



The noble gas halide bond is no longer stable after this mechanism has taken place. It thus decomposes into a noble gas atom and a halogen atom within a number of picoseconds after the actual laser process. In order to initiate this process, the gas mixture is brought between two high-voltage electrodes and excited by an electric discharge.

The electric discharge can be classified into two stages: first, free electrons are generated between the electrodes by a primary discharge, allowing a homogenous ignition by the subsequent main discharge. As a result of this principle of excitation, excimer lasers can only be operated in the pulsed regime where the pulse duration typically amounts to ten to some hundreds of nanoseconds. Even though buffer gases, for example helium or neon, are further added to the actual laser active gas mixture in order to increase the efficiency of the laser process, the degree of efficiency of excimer lasers is quite low and merely amounts to 2-4%. However, this type of laser allows the generation of discrete laser wavelengths in a broad UV wavelength range as listed in the Table 2.1.

2.4.4 Design of Excimer laser

The first experimental evidence of excimer lasing was obtained by N.G. Basov et. al 1970³⁰. They used a high-current electron beam to excite liquid Xe . Other excimer lasers were discovered after the investigation of fluorescence spectra of the rare-gas monohalides. The German start-up company Lambda Physik developed and manufactured its first commercial excimer laser, the EMG 500, the commercial multi-gas laser, which was introduced into the market in 1977. Since then, it is the major supplier of laser devices in the world. The Excimer laser device used in our PLD system is also from is from Coherence which was earlier known as Lambda Physik. The interior view of the laser device in shown in the Fig. 2.14

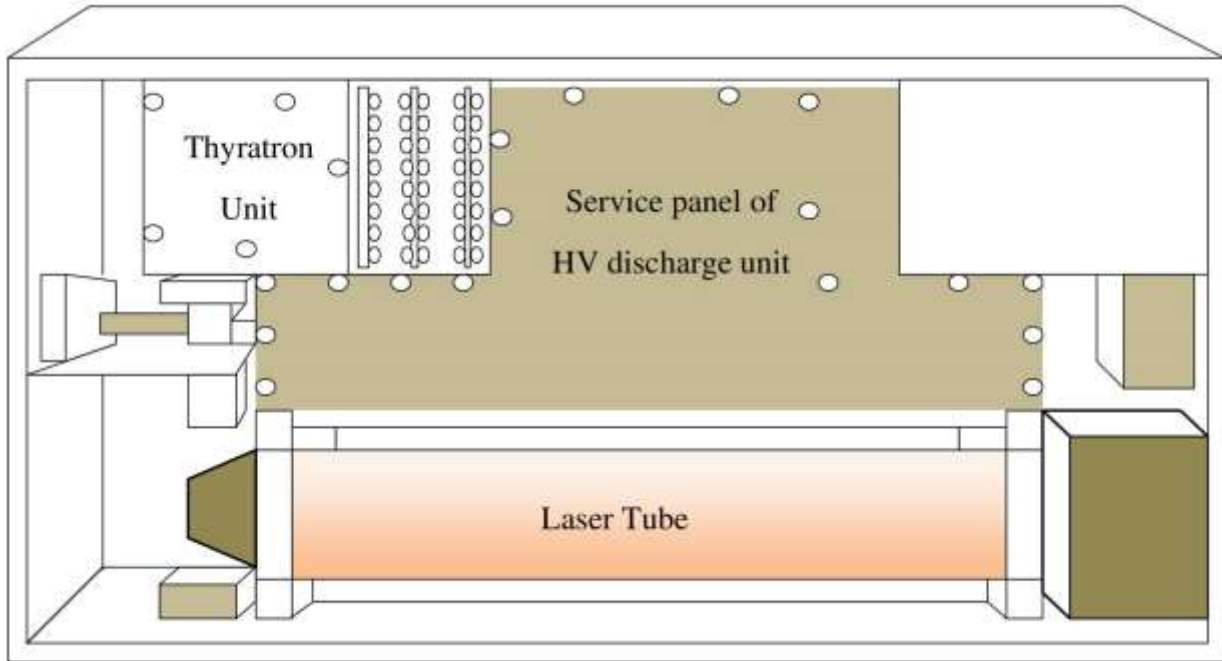


Fig. 2.14.: The interior view of the Coherent excimer laser device. The main components of the device are: thyatron, service panel HV discharge unit and the laser tube.⁴⁶

The components required for the lasing action are shown in the Fig 2.15. The functional design of the COMPexPro laser consists of the following primary components (Fig 2.15 A): A laser tube (A), high voltage power supply (B), thyatron (C), front mirror (partly reflective), rear mirror (highly reflective), capacitor array (F), communication interface (G), energy monitor (H) and the vacuum pump (I).

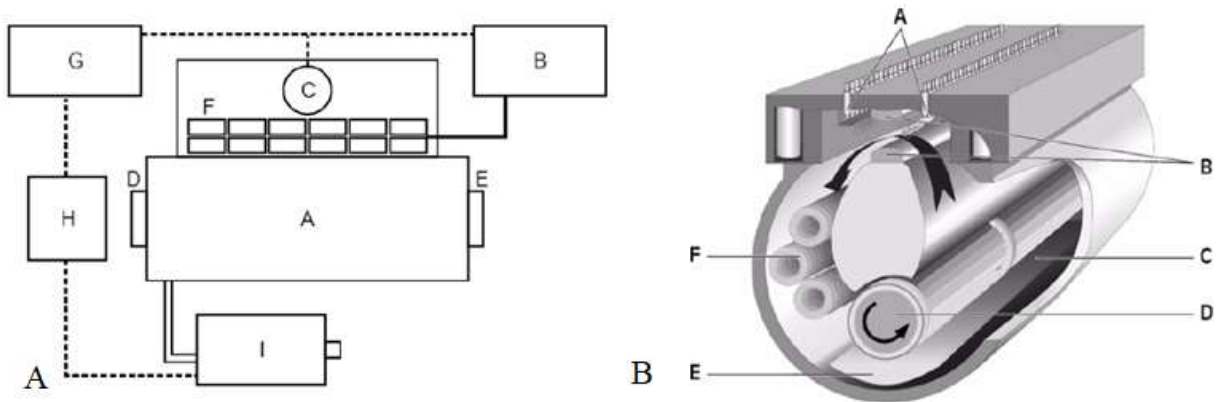


Fig. 2.15: A) A schematic diagram showing the primary components of the Coherent excimer laser.⁴⁶ B) Schematic diagram of the laser tube of the Coherent excimer laser device.⁴⁶

The laser tube is the heart of the laser device it can also be considered as the motor of the laser. Fig. 2.15 B shows a cutaway drawing of the longitudinally symmetrical laser tube. The laser tube (c) is the reservoir for the laser gas.

A high voltage discharge between the electrodes (B) transfers the energy of the excimer gas mixture (e.g. fluorine or krypton premix). This high voltage is generated by charging the storage capacitors and discharging by a thyatron. In order to obtain a controlled, spark-free discharge, the laser gas has to be pre-ionized, i.e. a sufficiently high density of free charged molecules has to be created between the electrodes. This is achieved with pre-ionization pins (A) arranged along the main electrodes. The result is a homogenous pre-ionization of the laser gas. The switching of pre-ionization and main discharge in series ensures a perfect synchronization between pre-ionization and main discharge.

After the high-voltage discharge, thermal inhomogeneities in the laser gas arise in the discharge area. Therefore, the gas volume in the discharge area has to be completely exchanged between two laser pulses. A transverse circulation fan (D) positioned within the laser tube causes the gas volume between the main electrodes to be completely replaced between two successive laser pulses. The circulation fan is driven externally via a magnetic coupling by a single-phase motor.

The energy efficiency of the excimer laser is to the order of 2%, i.e. the main part of the energy supplied has to be carried away in the form of heat. The gas, heated up by the discharge, reaches the heat exchangers (F) as a result of the flow in the laser tube and is cooled down to the correct operating temperature (approx. 30 degree C).

Each discharge pulse of the laser results in a load on the pre-ionization pins and main electrodes and causes a slight erosion of material. Precipitation of the created particles on the laser windows would result in diminishing beam intensity by scattering and absorption. These particles must permanently be removed from the laser gas which is done by an electrostatic filter (E) integrated in the gas circulation. Due to the pressure conditions generated by the circulation fan, the laser gas continuously flows through this electrostatic filter.

2.5 Vacuum System

2.5.1 Introduction

A vacuum is a space from which air or other gas has been removed; it is basically absence of matter. All the gas cannot be removed, that is, a perfect or absolute vacuum, which implies a space that is entirely devoid of matter is practically unrealizable and even the outer space is not a perfect vacuum. For practical purposes, the American Vacuum Society proposed a definition for the term vacuum as a space filled with a gas at least less than one atmospheric pressure³¹. In the traditional measurement system, normal pressure is expressed in millimeters of a column of mercury, and 760 millimeters of mercury is equal to 1 standard atmosphere. There are many different measurement units which are generally used, however, the unit, torr (1 millimeter of mercury) is the most widely used units of pressure but in our system we have used mbar.

The amount of vacuum generated depends on the application, and is done for many reasons. The main reason for the need of vacuum is to provide a clean surface in an experiment because at atmospheric pressure molecules constantly bombard surfaces. These molecules can bounce from surfaces, attach themselves to surfaces, or perhaps chemically react with surfaces. Air or other surrounding gas quickly contaminates a cleaned surface. A cleaner surface will remain clean in an ultra high vacuum chamber for longer periods of time, because the rate of bombardment is low. Another reason for having a vacuum is to make a molecule to travel from one wall of a chamber to another without colliding with many molecules. By reducing the pressure to suitably low value, a molecule from one wall can travel to another without a collision. Many effects become possible if molecules can travel long distances between collisions. The average distance travelled by a gas molecule or other particle between collisions with other particles is termed as mean free path. As the pressure inside the chamber decreases, the mean free path the gas molecules increases and the gas flow takes different forms.

2.5.2 Vacuum Fundamentals

Pressure Regions of vacuum

Measuring a system's pressure is the traditional way to classify the degree of vacuum. Nowadays, the general term *vacuum* refers to a region that consists of about eight orders of magnitude of pressure below 1 atmosphere. For convenience, this extended pressure range is generally divided into several regions that denote the *degree* of vacuum. This division of the pressure scale below the atmospheric pressure is somewhat arbitrary and is a convenient method of denoting the different physical phenomena that occur within the pressure ranges specified for each category. Many industrial applications of vacuum can be also be classified using these categories.

Degree of vacuum	Pressure range (mbar)
Atmospheric pressure	1013
Low (or Rough)	$10^3 - 33$
Medium	$33 - 10^{-3}$
High	$10^{-3} - 10^{-9}$
Ultra High	$10^{-9} - 10^{-12}$
Extreme Ultra High	$< 10^{-12}$
Outer Space	$10^{-6} - 10^{-17}$
Perfect vacuum	0

Table 2.2: *The accepted categories of the vacuum with the corresponding pressure ranges*³².

Flow Regimes

The production and maintenance of vacuum involves flow of gas from the vacuum vessel through pipelines and pumps to the atmosphere. The gas flow through the pipes takes different forms as the pressure starts decreasing (whereby the mean free path of the particles increases) in the pumping process. There are three types of flow that are mainly encountered in vacuum technology: viscous or continuous flow, molecular flow and at the transition between these is the Knudsen flow³².

(a) Viscous or continuum flow

This will be found almost exclusively in the rough vacuum range. The character of this type of flow is determined by the interaction of the molecules. Consequently internal friction, the viscosity of the flowing substance, is a major factor. If vortex motion appears in the streaming process, one speaks of turbulent flow. If various layers of the flowing medium slide over the other, then the term laminar flow or layer flux may be applied. Viscous flow will generally be found where the molecules' mean free path is considerably shorter than the diameter of the pipe.

(b) Molecular flow

The molecular flow prevails in the high and ultrahigh vacuum ranges. In these regimes the molecules can move freely, without any mutual interference. Molecular flow is present where the mean free path length for a particle is very much larger than the diameter of the pipe.

(c) Knudsen flow

The transition range between viscous flow and molecular flow is known as Knudsen flow. It is prevalent in the medium vacuum range. Knudsen flow is present where the mean free path length is comparable with the pipe diameter.

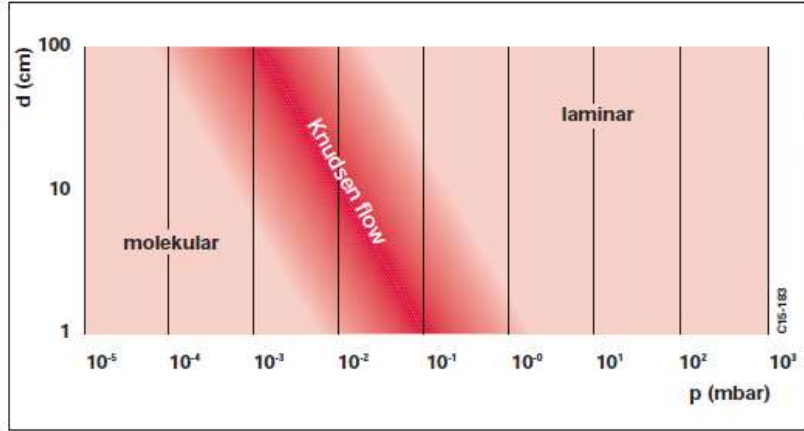


Fig. 2.16: Graph of pipe diameter, d versus pressure, P showing different flow regimes in the pipe with the variation of pressure of the gas³².

2.5.3 Generation of Vacuum

Vacuum is generated by means of pumping out the gas from the chamber. There are a variety of mechanical pumps available at the present time for the evacuation of a vessel. Most common are rotary vane and rotary piston positive displacement pumps (Fig. 2.17), and these are usually limited to a lowest inlet pressure. To achieve high vacuum, a turbo-molecular pump is used. It cannot create high vacuum all by itself but it requires a roughing pump (rotary pump) which generates fore vacuum for the inlet of the turbo. In the following sections we will look at the working of the turbo pump and the basic principle of vacuum measurement^{32,33}.

Vacuum system for Pulsed Laser Deposition

The vacuum system for Pulsed Laser Deposition consists of a vacuum chamber (excel instruments, Mumbai), turbo-molecular pump, oil-sealed rotary vane pump, gauges for measuring the vacuum and operating system. Pulsed Laser Deposition requires a high vacuum; for this, the pumps are used in combination to create high vacuum in the chamber. Whereas, the turbo-molecular pump, with the input pressure, generated by rotary, can achieve vacuum in high vacuum range of 10^{-6} mbar. The rotary and turbo are Pfeiffer based vacuum pumps. Rotary pump creates a fore vacuum in the range of 6×10^{-3} mbar for the turbo-molecular pump. Therefore, the rotary pump is also called as a roughing or backing pump for the turbo pump. There are two gauges used in the system, one for low vacuum and another for the high vacuum measurements. The cold cathode gauge is used to measure high vacuum ($10^{-2} - 10^{-9}$ mbar) and the thermal conductivity gauge (which is also a Pirani gauge) is used to measure low vacuum ($1000 - 10^{-4}$ mbar). The typical vacuum system for PLD is shown in the Fig.1.18.



Fig.2.17: A) A Hipace 300, turbo-molecular pumped in our UHV chamber³⁴. B) An oil-sealed rotary pump³⁵.

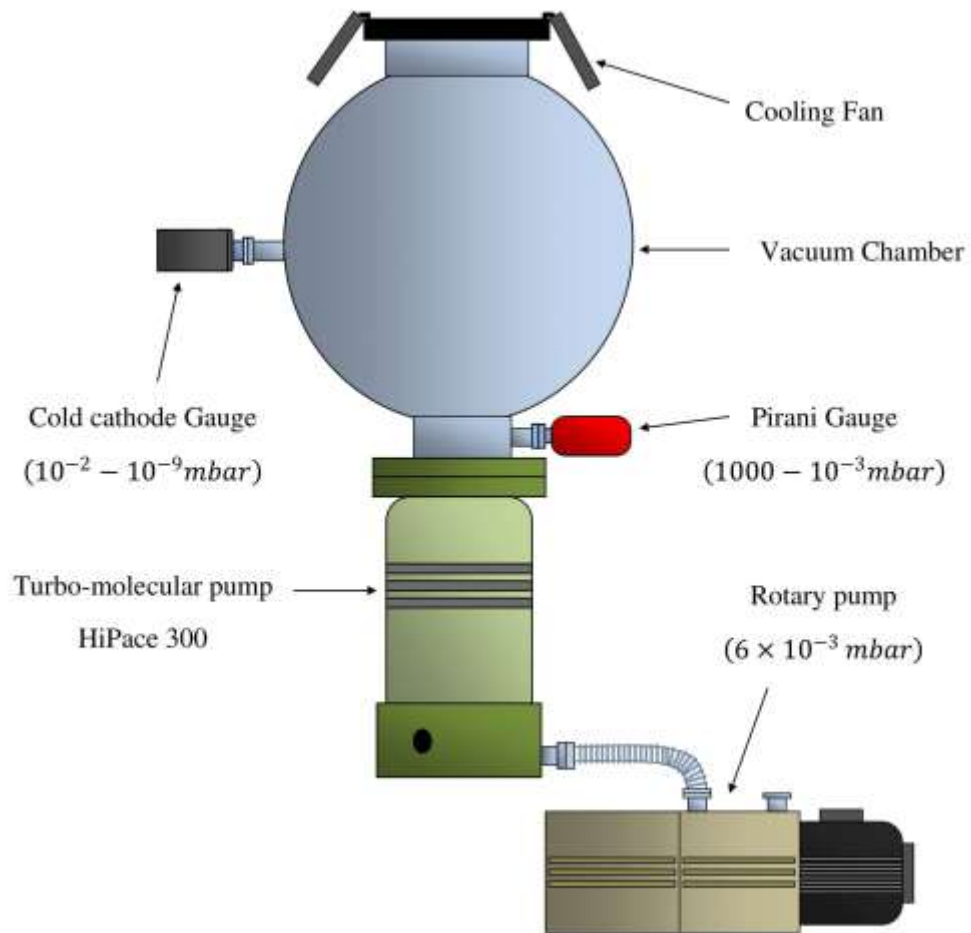


Fig. 1.18: A schematic diagram of the typical vacuum system used in pulsed laser deposition.

Turbo Molecular Pump and its Working Principle

The turbomolecular pump (TMP) invented by Becker in 1957 became commercially available in 1958. Since then it has become very popular in every field of high- and ultra-high-vacuum technique, due to the clean, consistent, and predictable vacuum created, the easy operation, and the advanced degree of operating reliability. It essentially comprises of a casing with a rotor and a stator with blades (or disks) attached to them. They are machined from a single block of high strength aluminum alloy. The turbo pump includes stationary rows of stator blades in between each row of rotor blades. The angle of the stator blades are opposite of the rotor blades and these angles are optimized to make it more probably for a gas molecule to move in the pumping direction rather than back flow in the opposite direction through the pump.

The turbomolecular pumping action can be thought of as a combined work of both the rotor and stator blades; they together form a pump stage and generate a compression ratio (for air ~30) for the gas molecules which enter through the inlet.



Fig. 2.19: A) Diagram showing the arrangement of the rotor and stator blades. B) The rotor blades of the turbo pumps down gas molecules out of the chamber³³.

The rotor blades hit the molecules and transfer the rotor impulse to the molecules by the superposition of the thermal velocity of colliding particles with the velocity component of the moving rotor surface. With the newly acquired momentum, the gas molecules accelerate along the pumping axis. The stator blades then decrease the velocity of the pumped gas. This is required so that the next row of rotor blades can impart additional velocity to the molecules moving them again farther along the pumping axis. This process is continued resulting in the multiplication of the compression effect by the sequential switching of several pump stages (modern turbomolecular pump rotors are designed with nine or more blade rows) attaining high compression ratios before the gas molecules finally expelled through the exhaust.

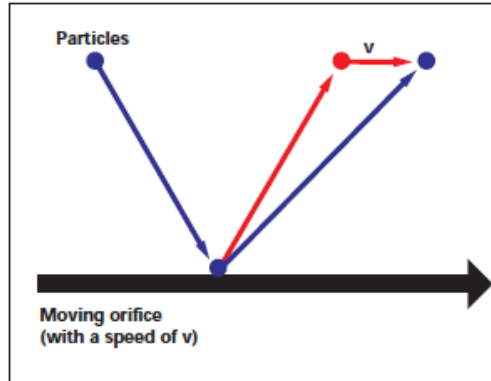


Fig. 2.20: When a gas molecule comes in contact with the rotor blade it gains velocity (or momentum)³².

The blades nearest to the intake of the pump are designed to have a high pumping speed and lower compression ratio since they will be pumping gas molecules at low pressure. As the gas molecules pass through the turbo pump they are compressed and therefore the blades nearest to the turbo exhaust are designed for high compression and low pumping speed.

The blade tip velocity of the turbo-molecular pump rotor has to be on the order of thermal molecular velocities. This high tip speed requires that turbo pumps operate at high rotational speeds. The angular frequency is dependent on the rotor diameter, such that, smaller turbo rotors are required to rotate faster than larger pumps, e.g., small turbo-molecular pumps often rotate between 70,000 and 90,000 rpm. Higher tip velocity provides better pump performance through higher gas compression which results in a lower ultimate pressure. For this reason, the blades of turbo-molecular pumps do not go to the center of the pump as area closer to the center of the pump will have slower speed and lower compression. For these reasons, turbo pumps are designed with blade length no longer than 30% of the rotor diameter. Turbo pump designs are also optimized to prevent back-flow between the rotor and stators along with preventing leakage around rotor blade tips.

When the mean free path of the particles is larger than the spacing between rotor and stator blades, particles collide primarily with the rotor, resulting in an efficient pumping process, and there is no interacting influence of the different gases. In the laminar flow range, the action of the rotor is diminished by the frequent collisions between the particles. Therefore, normally, a TMP is not capable of pumping gases against atmospheric pressure and must be backed by an adequate roughing pump.

2.5.4 Vacuum measurement

The ultra-high vacuum chamber of PLD system is fitted with two vacuum gauges, Cold cathode gauge and Pirani gauge which measure the pressure inside the chamber. The Pirani gauge is used for low vacuum ($1000 - 10^{-3} \text{ mbar}$) and Cold cathode gauge is used for high vacuum ($10^{-2} - 10^{-9} \text{ mbar}$). In this section we discuss the working principle these two gauges in brief.

Pirani gauge

The Pirani gauge (Fig. 1.21 A) which is named after its inventor, Marcello Pirani, is a thermal conductivity gauge. It consists of a hot metal wire usually made of Tungsten, Nickel or Platinum, suspended in a tube that is exposed to gas pressure of the chamber. The Pirani gauge measures the vacuum by monitoring the heat transfer from the wire to the surrounding gas.

The Pirani wire filament is connected to one leg of the Wheatstone bridge (Fig. 2.21 B); the other three elements are set for balancing and temperature compensation of the bridge circuit. The filament wire is maintained at a constant temperature and when the gas density changes and thereby thermal conductivity changes the energy required to maintain the wire changes accordingly. Consequently, the voltage supply to the Wheatstone bridge becomes vacuum pressure dependent and the measured bridge voltage can be converted to a pressure value.

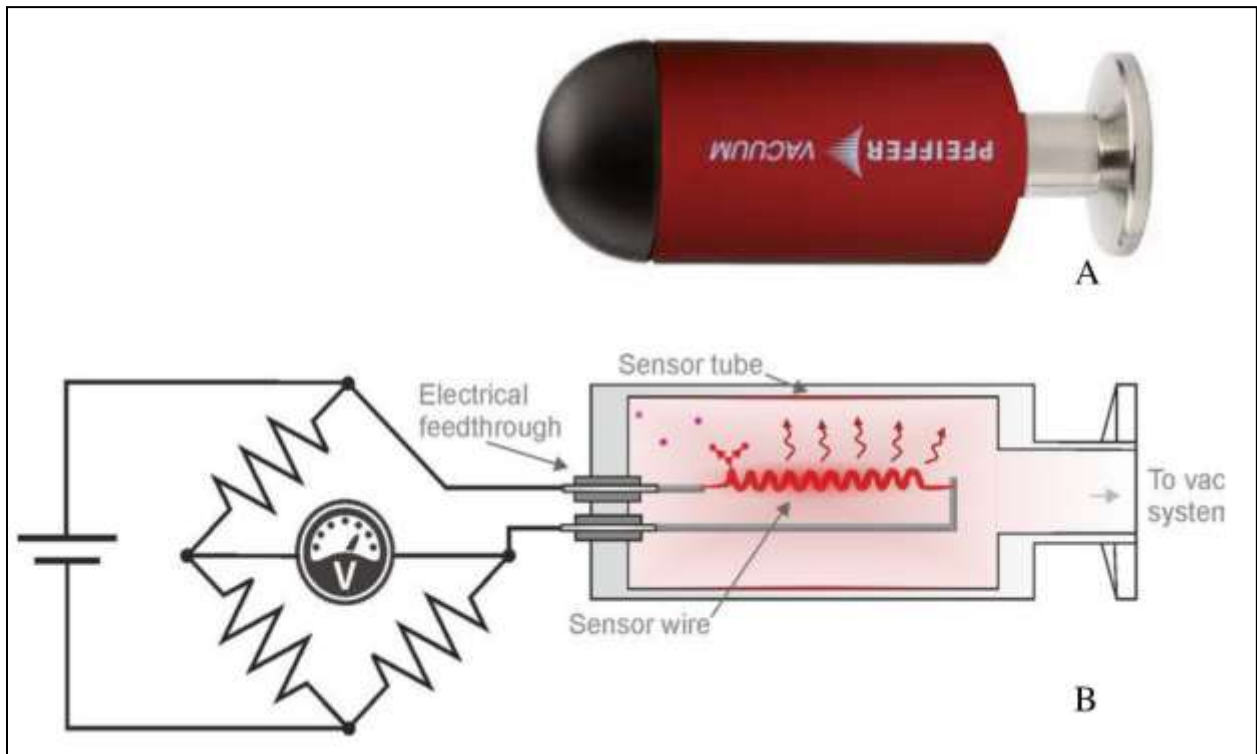


Fig. 2.21: A) A Pirani gauge for the measurement of low vacuum³⁶. B) A schematic diagram of the working principle of the Pirani gauge³⁷.

When the gas molecules collide with the hot wire, heat is transferred to the molecules from the hot wire. If the gas pressure is reduced the number of molecules present will fall proportionately and the wire will lose heat more slowly. Thus, the heat loss is a function of the gas pressure and at low pressure the low gas density and long mean free path between gas molecules provides a low thermal conductivity. At high pressure the high gas density and short mean free path between molecules will result in high thermal conductivity.

Cold-cathode gauge

Cold cathode ionization vacuum gauge essentially consists of only two electrodes, a cathode and an anode, between which a high voltage is applied. Negatively charged electrons leave the cathode through field emission, moving at high velocity from the cathode toward the anode. As they travel this path, they ionize neutral gas molecules, which induce a gas discharge. The measured gas discharge current is a function of pressure. However, only few molecules are ionized in the case of straight electron trajectories, which results in lower sensitivity. To avoid this disadvantage, the anode is surrounded by cylindrical cathode (which also forms measurement chamber, (Fig. 2.22) and an axially magnetized cylindrical, permanent-magnet ring is placed on the exterior of the cathode to generate a magnetic field within the chamber. The electrons travel through the magnetic field on spiral trajectories. The electron paths extended in this manner increase the probability of collisions with the gas molecules and ensure that sufficient ions are generated to maintain the gas discharge.

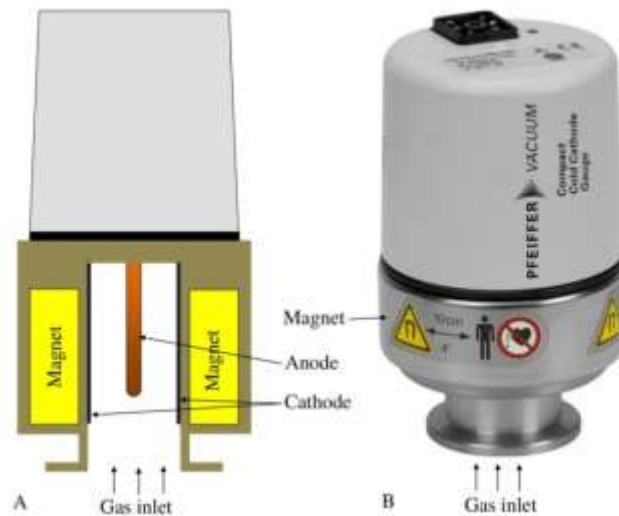


Fig. 2.22: A) A schematic diagram of the Cold cathode gauge showing the internal components. B) A cold cathode gauge used for measuring high and ultra-high vacuum³⁸.

CHAPTER 3

ELECTROCHEMICAL ANODIZATION OF TiO₂

3.1 Introduction

Electrochemical anodization is a versatile method for the formation of a thick oxide layer on a metal surface under optimized electrochemical treatments. Such thick oxide layers are corrosion and abrasion resistant, enhancing the hardness of a material along with their adhesion properties. Anodizing is basically a matter of highly controlled oxidation. Self-organized oxide pores and oxide tube arrays can be grown by anodization of a suitable metal. By using various metals, different oxide morphologies are obtained. The formation of nanotubes, degree of self-organization, tube dimensions, properties of nanotubes, tube length, pore diameter, thickness, and morphology of TiO₂ films can be easily controlled by the anodization parameters. During the anodization process, the color of the Ti plate changes due to the increase in thickness of TiO₂.

A compact oxide layer of considerable thickness is grown at the anode in a suitable electrolyte, where growth is proportional to the applied potential. TiO₂ is very stable in neutral electrolytes and with decreasing pH its dissolution rate increases. The anodic oxidation of the metal surface is also controllable, making it a cost-effective process. Tubes prepared by this method have a good surface adherent strength. A completely different morphology of the oxide can be seen by introducing electrolytes containing fluoride ions. Further, by annealing the substrates to certain temperatures, different phases of the crystalline materials can be obtained. It does not only influence the phase change, but also affects the morphology.

RBA (rapid breakdown anodization) is a process of formation of nanotubes in which random growth of nanotubes is observed, which are less organized. They grow in bundles within tens of seconds and are generally non-substrate-adherent. 1-Dimensional TiO₂ nanostructures can also be synthesized by various other methods such as sol-gel method, hydro/solvothermal method, template-assisted methods and by other electrochemical means. Anodization is also used for creating nanoporous templates for various applications in nanotech. Materials in nanoscience have gained importance in recent technology due to their high performance, which is determined by the geometry and morphology of nanostructures.

3.2 Apparatus

The electrochemical setup basically comprises of a beaker containing an electrolyte, two plates; anode and cathode, power supply and a digital multimeter for current measurement. Low temperature experiment additionally includes a circulating chiller bath and a double jacketed beaker. A typical apparatus for anodization is shown in the figure below.

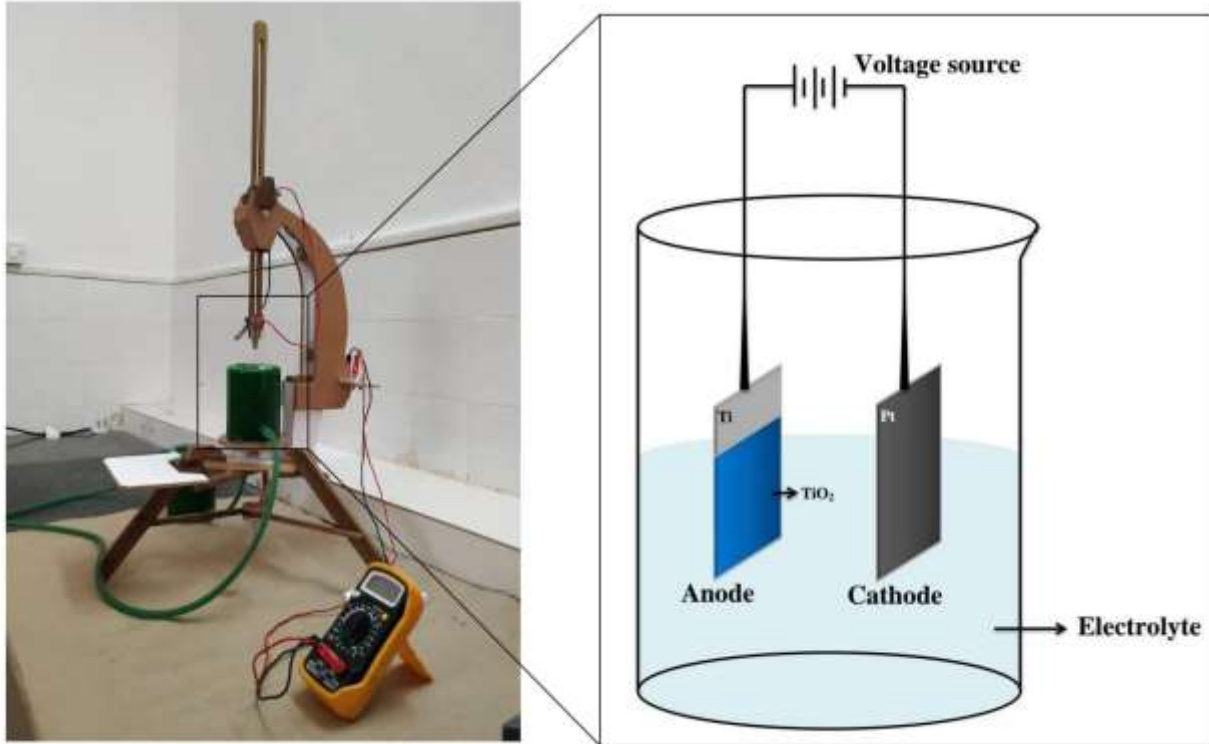


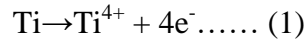
Fig. 3.1: Anodization apparatus.

3.3 Stages involved in TiO₂ nanotube growth

The formation of nanotube layer by anodization was carried out in potentiostatic mode at 40V. The potential range for aqueous electrolyte is 1-30V and for non-aqueous electrolytes is 5-150V, containing approximately 0.1–1 wt.% fluoride ions³⁹. The growth of oxide layer can be interpreted by recording the current-time characteristics and plotting a graph of current density (j) v/s time(s) as shown in Fig. 3.5. Anodizing is achieved by halfway-immersing the titanium plate (anode) and platinum plate (cathode) into an electrolyte bath and applying a constant voltage to it. Since titanium acts as the anode, oxygen ions released from the electrolyte combine

with the titanium atoms at the surface of the part being anodized and forms an oxide layer of finite thickness over it.

The anodization process involves the formation of ions such as Ti^{4+} , O^{2-} . The formation of TiO_2 nanotubes includes two competitive reactions: anodic oxide formation by oxygen anions (O_2^- and OH^-) and the chemical dissolution reaction caused by fluoride ions in the electrolyte⁴⁰. Equation (1) represents the formation of metal ion⁴³.



In the absence of fluoride ions in the electrolyte, a compact oxide layer is formed on the surface of TiO_2 due to the reaction of metal species with O^{2-} ions from H_2O . According to equation (2):

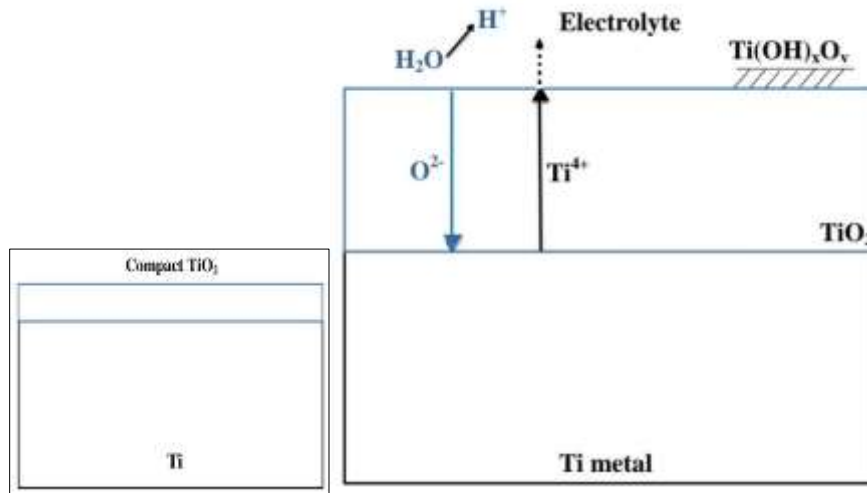


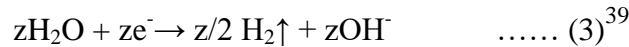
Fig. 3.2: A schematic diagram of oxide layer formation.³⁸

This oxide layer is formed due to the electrolysis of water, causing O_2^- and OH^- anions to evolve at the oxide-electrolyte interface. The field generated, causes the transport of these anions to the oxide-metal interface and simultaneously, Ti^{4+} ions diffuses through the oxide layer (in the opposite direction) towards the oxide-electrolyte interface and reacts with O_2^- ions, thus forming the TiO_2 layer⁴⁰. Therefore, the growth of the anodic oxide layer depends on the migration of ions (Ti^{4+} , O^{2-}) through the oxide layer aided by the field induced. As shown in Fig. 3.4.

Since the process is carried out in potentiostatic mode, the field inside the oxide is progressively reduced with the increasing oxide thickness. The exponential current decay is a result of the decreasing field strength⁴¹.

Hydroxide layer formation: if the incoming Ti^{4+} ions are not made soluble at the oxide-electrolyte interface by complexation, a precipitate will be formed in the electrolyte which is loose porous. It has no contribution in the field but it affects the diffusion rate⁴¹.

A counter reaction which takes place simultaneously at the cathode with hydrogen being evolved is given by equation (3):



Electrolytes containing fluoride ions strongly affect the anodization process. The rate of migration of F^- ions through the oxide is twice as that of O^{2-} ions, (due to the smaller ionic radii of the F^- ions) therefore they can react with Ti^{4+} at the oxide-metal interface⁴¹.

F^- ions react with Ti/TiO_2 to form water soluble titanium fluoride complex $[TiF_6]^{2-}$. This complex is easily dissolved in electrolyte due to its high solubility in water. Complexation occurs with Ti^{4+} ions, ejected at the oxide-electrolyte interface (after migration through the oxide layer) and by (permanent) chemical attack of the formed TiO_2 and prevents precipitation as Ti^{4+} ions arriving at the oxide-electrolyte interface is solvated to $[TiF_6]^{2-}$ as shown in the following equations^{39,41}.



Equation (5) also represents the steady-state situation between the tube formation at the bottom and etching at the top surface.

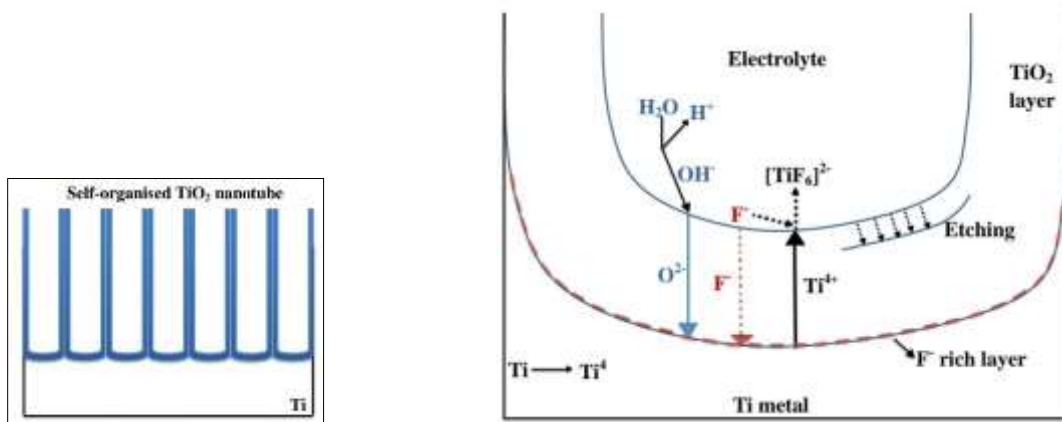


Fig. 3.3: A schematic diagram of tubular growth structure.⁴¹

The presence of F^- ions makes a honeycomb-like porous structure that transforms into an array of tubes with a F^- -rich layer between the TiO_2 layer and the Ti metal. This results in the formation of a hemispherical oxide-metal interfacial structure. The separation of this porous layer into tubes is due to good solubility of fluoride rich layer in water.

Tube ordering can be achieved by using a pre-structured surface that provides geometric requirement. By performing first step anodization, nanotubes are formed followed by the removal of tube layer and finally, a second step anodization. Here, the organized dimpled Ti metal surface after the removal of tube layer, acts as initiation sites for the tube growth in second step anodization.

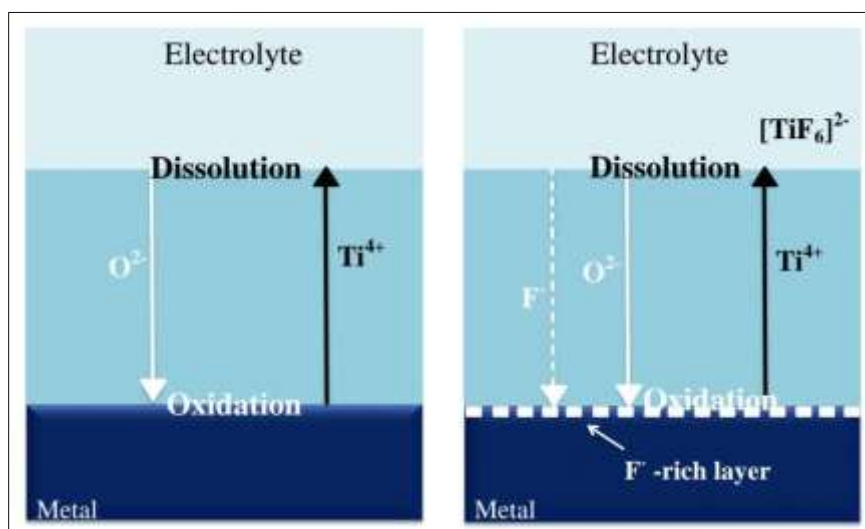


Fig. 3.4: A general diagram showing field aided transport of mobile ions through the oxide layer in the absence and presence of fluoride ions.³⁹

3.4 Role of fluoride ions

A key factor responsible for the electrochemically formed titanium nanotubes is the amount of fluoride ions present in the electrolyte⁴³. The fluoride ion concentration yields different oxide morphologies. The solubility of the fluoride rich layers in the electrolyte causes the separation of a porous layer into tubes.

Classification of fluoride concentration :

- 1) Low fluoride concentration (≤ 0.05 wt. %): a fluoride-ion free case is observed and a stable compact oxide layer is formed.
- 2) High fluoride concentration (1 wt. %): no oxide formation takes place as all Ti^{4+} formed reacts with abundant fluoride ions to form soluble $[\text{TiF}_6]^{2-}$.
- 3) Intermediate fluoride concentrations: a competition between oxide formation and Ti^{4+} solvatization takes place, leading to the formation of porous oxides or nanotubes³⁹.

Fluorides maintain a thinner bottom oxide layer by chemical etching of the oxide layer and solvatization of Ti^{4+} species at the oxide-electrolyte interface. Therefore the etching rate is determined by the fluoride and water concentrations in the electrolyte⁴⁰.

3.5 Theoretical explanation for the stages involved in anodization process

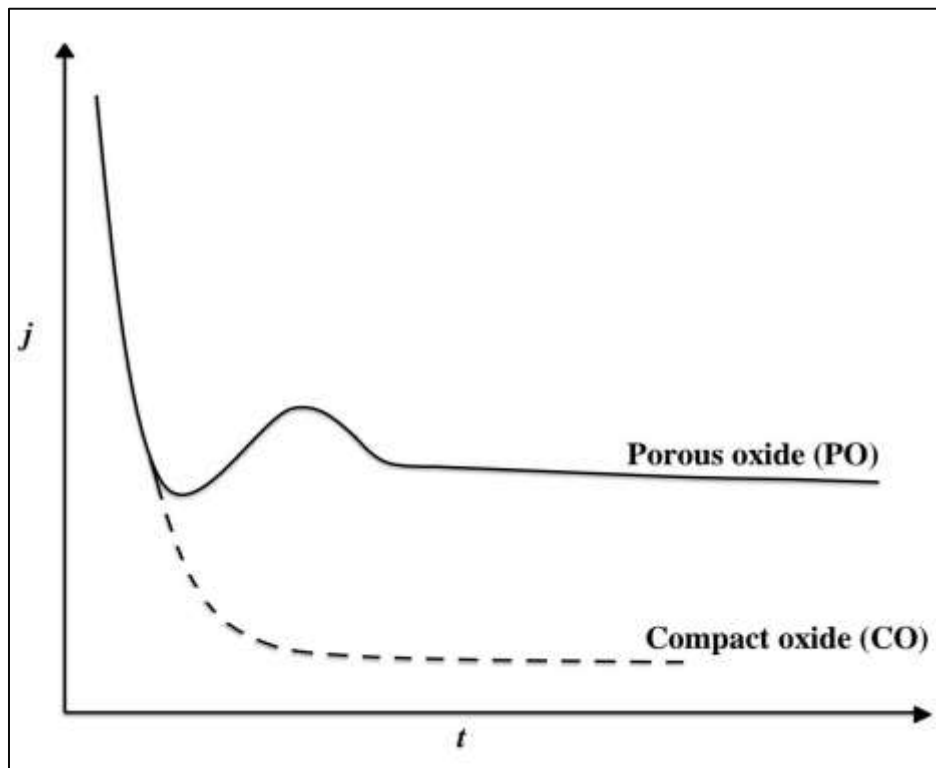


Fig. 3.5: A typical current-time curve after applying a voltage in the absence (.....) and presence (———) of fluoride ions.³⁹

The curve involves following three stages:

- I) In the initial phase of anodization, there is an exponential current decay caused by the barrier oxide layer formed on the surface of the sample. A fluoride free behaviour is observed.
- II) The current increases slightly due to formation of nano-sized pores, with a time lag caused by increasing surface area of deposition at the anode. With shorter time lag, the fluoride concentration will be higher due to fluoride induced dissolution of formed TiO_2 and pore formation.
- III) The initially formed irregular nanoscale pores penetrate the initial compact oxide, and a tubular structure begins to grow beneath the pores, due to which the current decreases again. When the pore growth rate at the metal oxide interface and induced dissolution rate of the formed TiO_2 at the outer interface reaches an equilibrium condition, the current then reaches a steady state ⁴².

3.6 Different stages involved in the Pore formation

There are three stages involved in the pore formation process.

In the 1st stage, a barrier oxide is formed leading to an exponential current decay. During 2nd stage, the surface becomes locally activated and pores start to fabricate randomly. In the 3rd stage, due to the pore growth the current increases. After sometime of pore formation, a tree like growth is observed. Hence, the individual pores start interfering with the neighbouring pores and compete for available current. This happens under optimized conditions leading to a situation where the current is shared equally amongst all the pores and self-ordering under steady state takes place ⁴².

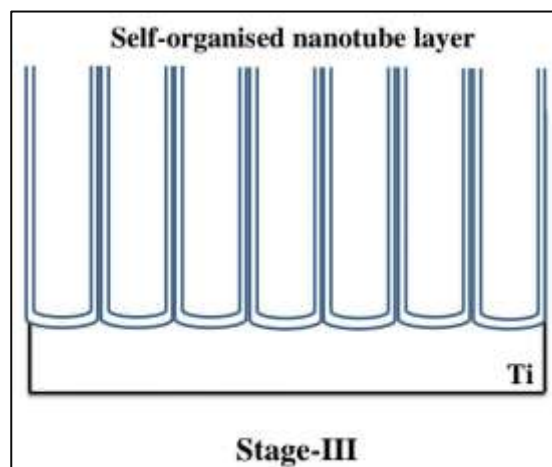
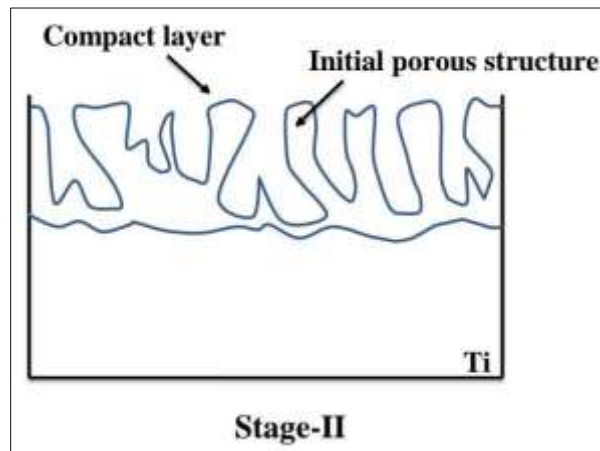
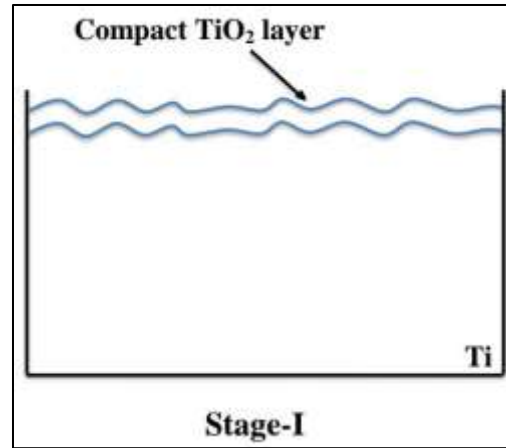


Fig. 3.6: The three different stages involved in the formation of TiO₂ nanotube arrays (I-III). Stage I: A barrier oxide layer is formed. Stage II: Pores start to grow randomly. Stage III: Formation of Self-organized nanotube layer.⁴²

3.7 Factors responsible for the change in geometry and composition

Different Titanium dioxide structures can be obtained by controlling the electrochemical anodization parameters of Titanium, such as a flat compact oxide, a disordered porous layer, a highly self-organized porous layer, and finally a highly self-organized nanotubular layer⁴³. The tube length or anodic layer thickness is defined by anodization time and etching rate. The diameter of the nanotubes is controlled linearly by the applied voltage.

Under steady-state conditions, the nano-tubular oxide layer thickness depends linearly on the anodization time, i.e. the charge passed during anodization. However, due to etching by the electrolyte, at some point an equilibrium state between the growth of the oxide and chemical dissolution takes place³⁹.

Applied voltage

The voltage is a strong parameter in controlling the diameter, inner pore distance of the nanotubes grown by anodization and it also influences film thickness. At low voltages the morphology of porous TiO₂ film is similar to that of porous alumina.

Variation of thickness with voltage:

When a constant voltage (U) is applied, the field (F) drops constantly and thus the driving force (for solid state ion migration) is reduced, which results in the increase of film thickness (d) given by:³⁹

$$F=U/d$$

This results in an exponential decay in current-time characteristics until the field effect is lost. Now, a finite thickness is achieved which mainly depends on the anodization voltage.

The final thickness is given by $d=fU$

where, f = growth factor of the oxide (2-4nm V⁻¹)³⁹

At low applied voltages, less electric field dissolution occurs forming smaller diameter TiO₂ nanotubes. If the voltage is too low, only a compact TiO₂ layer is formed and no nanotubes appear. However, a spongy-like porous structure is seen when the voltage is too high. At low voltages, tubes with few 100nm in length and few tens of nm in diameter can be obtained. For higher potential, formed nanotube layers are not self-organized. The level of diameter control grants various applications where the alteration of the diameter can be of specific use. For e.g. a defined size for embedding of biological species⁴². If applied potential is very high, dissolution rate may increase leading to permanent dissolution of oxide layer and hence no tubes will be formed.

Electrolyte:

The nature of the electrolyte strongly affects the formed structure. Under same conditions, different electrolyte can produce different electric field intensities which results in difference in morphology and composition of the nanotubes grown. Synthesis of nanotubes can be carried out either in organic electrolyte or aqueous electrolyte. Fluoride rich electrolyte such as $\text{NH}_4\text{F}/\text{CH}_3\text{COOH}$, $\text{H}_2\text{SO}_4/\text{HF}$, $\text{Na}_2\text{HPO}_4/\text{NaF}$ or the organic electrolyte like $(\text{NH}_4)_2\text{HPO}_4/\text{NH}_4\text{F}$ and $(\text{NH}_4)_2\text{SO}_4/\text{NH}_4\text{F}$ can be used. Titanium nanotubes can also be synthesized in fluoride free electrolytes such as perchlorate and chloride containing electrolytes⁴².

Etching: The etching rate depends on the type of electrolyte. In acidic electrolytes, etching is faster and tube length is limited to 500-600nm. In neutral electrolytes, the thickness is much more than in acidic conditions, and the layer thickness ranges from 2-4 μm (due to reduced chemical dissolution). Chemical dissolution can be further decreased in glycerol or ethylene glycol based organic electrolytes. In long duration anodization experiments, the etching of tubes at their top may cause inhomogeneous top structure and collapsing and bundling tube tops may appear.

The **water content** in the electrolyte also affects the growth rate of the oxide layer (tube bottom) and chemical dissolution of the nanotubes. Organic electrolyte has a small amount of water content. Whereas in aqueous electrolytes there is high water content which results in the formation of ripples at the side walls of the nanotubes. In Organic electrolyte, long and self-organised tubes with smooth tube walls can be grown upto large diameters (up to 700nm) since the tube splitting is controlled by low water content. **Inner tube layer:** in some organic electrolytes, and for higher voltage anodization, the inner tube layer shows high uptake of carbon from the electrolyte due to decomposition of organic electrolyte. Whereas, in aqueous electrolyte the inner tube is hydroxide rich than the outer layer⁴³. A V-shaped tubular morphology is present for both types of electrolytes i.e. Aqueous and non-Aqueous electrolytes³⁹ as shown in Fig. 3.7

Tube morphology

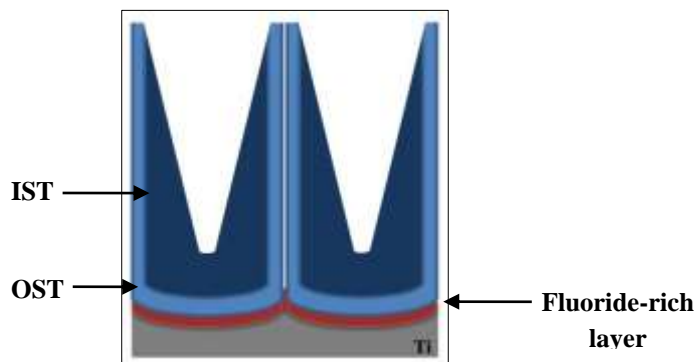


Fig. 3.7: Structure of typical TiO_2 nanotube formed in organic electrolyte.³⁹

The nanotube layer grown in fluoride containing electrolyte, show a V-shaped morphology. This is due to exposure of tubes to fluoride-containing electrolyte responsible for permanent etching and thinning of tube walls. The general shape as shown in Fig. 3.7 describes the composition distribution of tubes. The inner part of the shell (IST) is of a more loose nature and consists of incorporated electrolyte constituents, and the outer part of the tube is generally dense and very pure TiO₂³⁹.

Effect of pH of Electrolyte

The effect of pH alters the self-organization behaviour of titanium nanotubes. The difference in pH causes variations in thickness and in turn the pore diameter. At low pH the dissolution rate is greater than that of the higher pH i.e. the etching rate is faster in acidic electrolytes. In case of neutral electrolyte, the layer thickness is much more due to the reduced chemical dissolution. Thus, the chemical dissolution rate of TiO₂ is a highly pH dependent process⁴³.

Chemical dissolution can be further reduced by carrying out the anodization process in glycerol or ethylene glycol based electrolytes. In such electrolytes linear growth behavior could be extended³⁹.

Annealing: (change in phase structure)

The as-formed TiO₂ nanotubes have an amorphous nature. The nanotubes can be converted to various crystalline forms such as anatase, mixture of anatase and rutile, or rutile by annealing at higher temperatures. Annealing can be carried out in oxygen rich environment such as air or O₂ or in different gas atmospheres such as N₂, or a N₂/H₂ mixture that leads to different anatase-rutile ratios of TiO₂. A significant conversion of nanotubes into anatase phase occurs approximately at 280°C. With an increasing annealing temperature up to a certain limit, the anatase formation can be enhanced. A mixture of anatase and rutile can be obtained at temperature above 450°C. Above 500°C rutile phase starts to form and it is seen that the nanotubular integrity is maintained below 600°C. Above this temperature the nanotubes are not stable and at higher temperatures the nanotube bundles start collapsing. Moreover, annealing at 700°C favors sintering and tends to destroy the nanostructure. Due to unfavorable conditions sometimes, cracks may develop in the tube walls³⁹.

Conductivity along the tubes is also affected by the heat treatment; hence appropriate duration of annealing of the substrate is required for different applications. The annealing duration and ramping speed also has a significant effect on the crystal structure and composition of the newly formed phase of TiO₂. **Formation of Ti³⁺:Ti³⁺** species may be formed during the heat treatments. Heat treatment carried out under vacuum or in the absence of O₂ environment leads to a loss of O₂ from the material and formation of Ti³⁺. The material formed shows visible light absorption

and enhanced conductivity. By heat treatments, approximately 1% of the lattice atoms may be reduced to Ti^{3+} . The effect of annealing temperature can be later observed from the tube wall morphology^{42,43}.

Anodization time dependence:The layer thickness is directly proportional to the anodization time. As the reaction proceeds, the conductivity of the electrolyte changes and thus variations in the diameter are observed for longer anodization time. The fastest growth conditions typically represent conditions for optimized ordering.

CHAPTER 4

CHARACTERIZATION TECHNIQUES

4.1 X-Ray Diffraction Technique

X-Ray diffraction is a powerful, non-destructive and common analytical technique for the study of structure, phase identification and atomic spacing of crystalline materials. It is also used to determine the thickness of thin films and multi-layers. By using precise lattice parameter measurement, the lattice miss-match of a thin films (or an epitaxial layer) and its substrate can be determined with great precision. The credit for the broad applications of XRD goes to Rontgen, Laue and Bragg. Rontgen discovered the X-rays in 1895; Based on the fact that wavelength of X-rays is comparable to the atomic spacing, Laue, in 1912 discovered that crystalline substances act as three-dimensional diffraction gratings for X-rays similar to the spacing of planes in a crystal lattice and finally, Bragg formulated the simple law for the constructive interference condition for the incident X-rays on the crystalline sample (Fig 4.1).

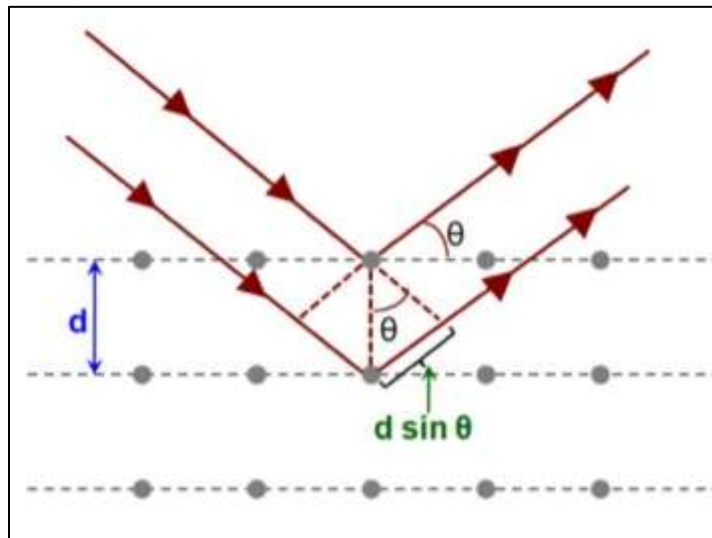


Fig. 4.1: *Bragg's law*⁴⁷.

The basic XRD method involves the generation of X-rays by a cathode ray tube, filtered to produce monochromatic radiation, collimated to concentrate, and directed toward the sample. The sample being crystalline, the incident X-rays interact with periodic lattice sites and produce constructive interference whenever the Bragg's condition is satisfied. For a periodic crystal lattice with inter-planar spacing, d and incident angle, θ of X-rays, the Bragg's law is given as

$$n\lambda = 2d \sin \theta$$

Where, n and λ are the numeric constants known as order of diffracted beams and characteristic wavelength of X-Rays impinging on the sample respectively. Each interference condition corresponds to a peak in the XRD pattern of a crystalline sample. The peak positions give all information about the crystal.

4.2 FTIR Spectroscopy

FTIR spectroscopy is an improved method of IR spectroscopy and where FTIR stands for Fourier Transform InfraRed. In infrared spectroscopy, IR radiation is passed through a sample, some of the infrared radiation is absorbed by the sample and some of it is passed through (transmitted). The resulting spectrum represents the molecular absorption or transmission, creating a molecular fingerprint of the sample. Like a fingerprint no two unique molecular structures produce the same infrared spectrum. This makes infrared spectroscopy useful for several types of analysis like, identification of unknown materials, determination of quality or consistency of a sample, determination of the number of components in a mixture, etc.

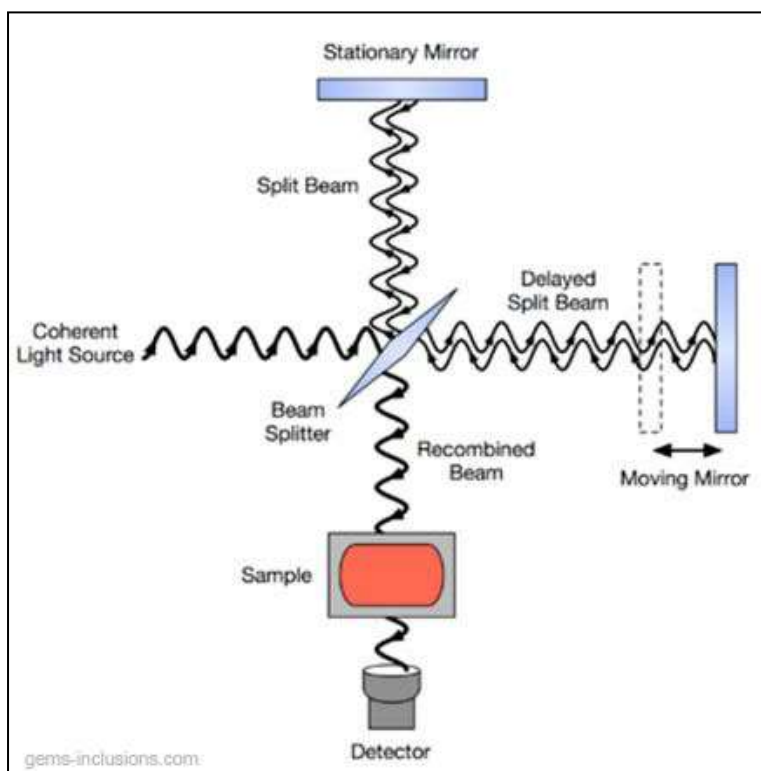


Fig. 4.2: Schematic diagram of FTIR spectrometer.⁴⁴

Originally, infrared spectrometers used a dispersive technique, which is basically a technique to separate the individual frequencies of energy from the infrared source by the use of a prism or

grating. An infrared prism works exactly the same as a visible prism which separates visible light into its colors (frequencies). A grating is a more modern dispersive element which better separates the frequencies of infrared energy. The IR radiation of individual frequencies is then incident on the sample. The detector measures the amount of energy at each frequency which has passed through the sample. This results in a spectrum which is a plot of intensity vs frequency. Since each individual frequency is checked for absorption one after the other, this technique is very time consuming in producing the absorption or transmission spectrum of the sample. To overcome this limitation a new technique has been developed, which employs the principle of interference and Fourier transform to measure all the infrared frequencies simultaneously which results in the quick generation of the absorption or transmittance spectrum of the sample.

An Interferometer (Fig. 4.2) is used for this purpose. It produces a unique type of signal which has all of the infrared frequencies “encoded” into it. Most interferometers employ a beam-splitter which takes the incoming infrared beam and divides it into two optical beams. One beam reflects off from a flat mirror which is fixed in place and the other beam reflects off from a flat mirror which is on a mechanism which allows this mirror to move a very short distance (typically a few millimeters) away from the beam-splitter. The two beams reflect off from their respective mirrors and are recombined when they meet back at the beam-splitter. Because the path that one beam travels is a fixed length and the other is constantly changing as its mirror moves, the signal which exits the interferometer is the result of these two beams “interfering” with each other. The resulting signal is called an interferogram which has the unique property that every data point (a function of the moving mirror position) which makes up the signal has information about every infrared frequency which comes from the source. The interferogram is then incident on the sample and the transmitted signals through the sample are detected by the detector. Since the transmitted signals are also an interferogram, they need to be converted to frequency form. This is done by Fourier transform of the measured interferogram to produce a frequency spectrum which is easy for analysis.

4.3 Scanning Electron Microscopy (SEM)

Scanning electron microscopy is a surface microscopy technique used for material characterization. SEM uses high energy electron beam, focused onto a sample to generate variety of signals of both photons and electrons such as X-rays, cathode-luminescence, auger electrons, primary back-scattered electrons, secondary electrons, etc at the surface of it, among which, secondary electron and back-scattered signals are commonly used for imaging the samples. SEM can generate high resolution (with a resolution better than 1 nanometer) images of shapes of objects (SEI) to study their morphology. It can also be used to determine crystalline structure, to show spatial variations in chemical compositions and other physical and chemical properties of a species.

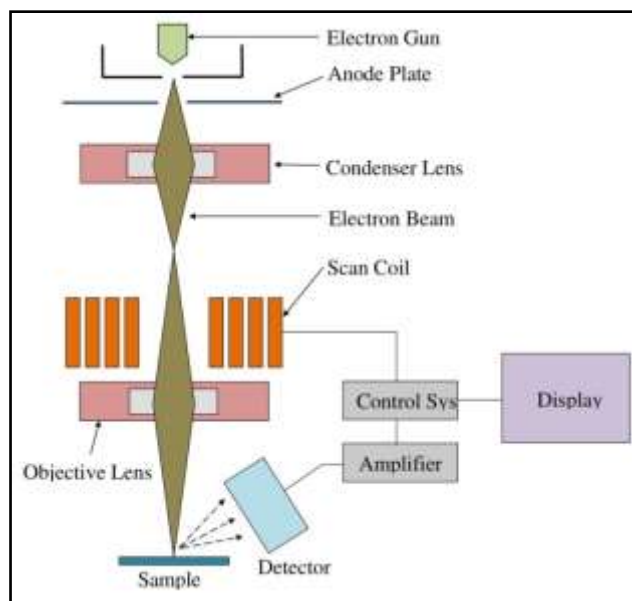


Fig. 4.3: Schematic diagram of the scanning electron microscope⁴⁸.

Electrons from an electron source (thermionic, Schottky or Field-emission cathode) are accelerated through a voltage difference between cathode and anode to generate a highly energetic electron beam. This beam of electrons is passed through various electro-magnetic lenses and apertures situated in the electron column to produce a finely focused beam of reduced diameter (also called an electron probe) on the surface of the specimen. A deflection coil system in front of the final lens field scans the electron probe in a raster across the specimen. The interaction between the electron beam and the sample produces different signals like secondary electrons, backscattered electrons, and characteristic X-rays. These outgoing signals are detected by various detectors and fed to the computer to form 2D image of the specimen (Fig. 4.3).

4.4 UV visible spectroscopy

Ultra Violet Visible spectroscopy is type of absorption spectroscopy which involves the absorption of ultra-violet light (200-400 nm) by chemical compounds, which results in the production of distinct spectra. When a chemical compound absorbs UV radiation, the molecules present in it undergo excitation. The energy of the UV radiation that is absorbed is equal to the energy difference between the ground state and higher energy states ($\Delta E = h\nu$). Generally, the most favored transition is from the highest occupied molecular orbital (HOMO) to lowest unoccupied molecular orbital (LUMO). The relation between absorption and intensity of the incident radiation is given by the Beer-Lambert's law, which states that, when a beam of monochromatic light is made incident on a solution that contains a substance that absorbs the monochromatic light, the rate at which the intensity of the beam decreases along the thickness of the solution is directly proportional to the concentration of the absorbing substance in the solution

and is also directly proportional to the intensity of the incident monochromatic radiation. From the Beer-Lambert law it is clear that greater the number of molecules capable of absorbing light of a given wavelength, the greater the extent of light absorption. This is the basic principle of UV spectroscopy. It is useful in the detection of functional groups, identification of unknown compounds, determination of purity of a substance, etc.

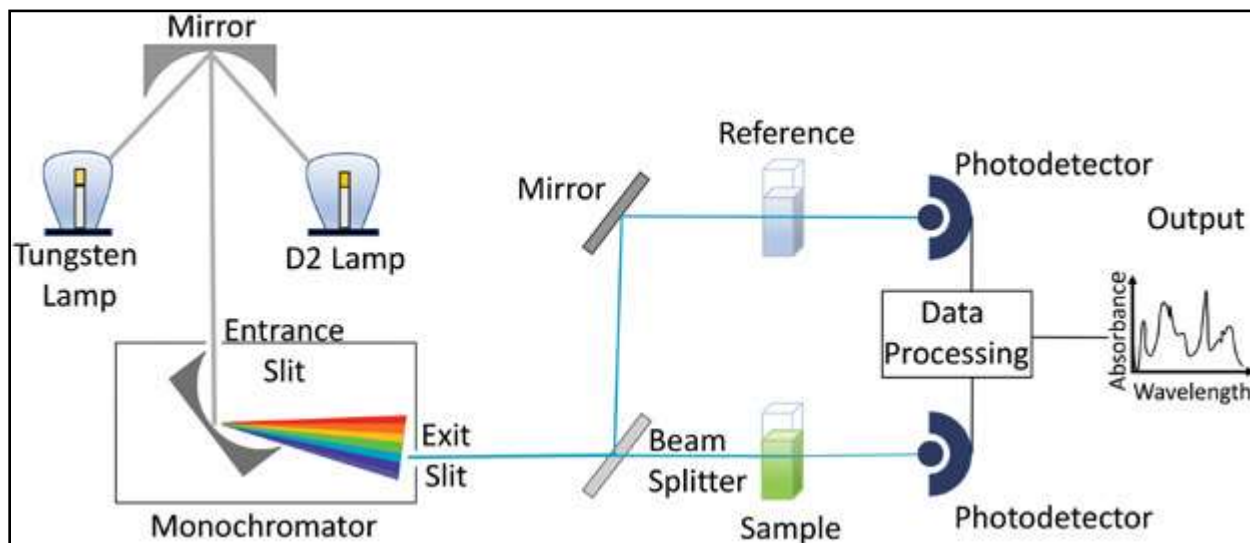


Fig. 4.4: Schematic diagram of UV spectrometer.⁴⁵

The basic components of the modern UV spectrometer (Fig.4.4) are the light source, monochromator, sample and reference cells, detector and amplifier. Tungsten filament lamps and Hydrogen-Dueterium lamps are mostly used as they cover the whole UV region. Tungsten filament lamps specifically emit the radiations of 375 nm and Hydrogen-Deuterium lamps emit radiation below 375 nm. Monochromators are generally composed of prisms and slits. The radiation emitted from the primary source is dispersed with the help of rotating prisms. The various wavelengths of the light source which are separated by the prism are then selected by the slits such the rotation of the prism results in a series of continuously increasing wavelength to pass through the slits for recording purpose. The beam selected by the slit is monochromatic and further divided into two beams with the help of another prism. One of the two divided beams is passed through the sample solution and second beam is passed through the reference solution. Both sample and reference solution is contained in the cells. These cells are made of either silica or quartz. Glass can't be used for the cells as it also absorbs light in the UV region.

There are two photocells in the spectrometer which serve the purpose of detection of the signals in the UV spectroscopy. One of the photocells receives the beam from sample cell and second detector receives the beam from the reference. The intensity of the radiation from the reference cell is stronger than the beam of sample cell. This results in the generation of pulsating or alternating currents in the photocells. The alternating current generated in the photocells is transferred to the amplifier where the weak signals from the photocells are amplified

many times to get clear and recordable signals. The signals are then processed by the computer to produce the spectrum of the desired compound.

CHAPTER 5

EXPERIMENTAL RESULTS AND DISCUSSIONS

5.1 Pulsed Laser Deposition

5.1.1 Introduction

Pulsed laser deposition (PLD) has emerged as an important technique of preparing thin films which can improve layer-by-layer growth. The growth process of thin films in pulsed laser deposition depends on a number of experimental parameters which dramatically affect the morphology, crystallinity, and composition of the deposited material. To obtain the good quality films with the desired properties, these parameters need to be optimized. The optimization of parameters involves the process of testing the effect of one parameter keeping the others constant which gives the better understanding of the role of that specific parameter in improving the quality of the film and its properties.

5.1.2 Observations

The observation Table 5.1 shows the parameters being studied for optimization. The common parameters studied are: pulse repetition rate (reprate), substrate temperature and pulse energy (laser fluence). As a part of the study it is also important to understand the operation of the laser device to have better control over pulse rate and energy of the laser. The Coherent excimer laser can be operated either in No Gas Replacement (NGR) or Partial Gas Replacement (PGR) condition. In each working condition there are two fundamental running modes -- Constant Energy (EGY CONST) and Constant High Voltage (HV CONST) mode. It often requires to switch the mode of operation for judicious use of the laser gas as it ages with time resulting in the decrease of pulse energy. The pulse energy (output energy) of an excimer laser is dependent upon the charging voltage (high voltage) and condition (age) of the excimer laser gas. When the pulse energy (E) is considered as a function of the charging voltage (U), the result is approximately the function shown in the Fig. 5.1 A. As excimer laser gases age, the pulse energy obtained from a given charging voltage will decrease. When the Energy Constant mode is selected, the laser control continuously adjusts the high voltage to achieve laser operation at a preset energy level (Fig. 5.1 B). When the HV Constant mode is selected, the pulse energy decreases with time as excimer laser gases have a limited lifetime (Fig.5.1 C). Regardless of the running mode used, the laser gas quality will reach a state which is insufficient to adjust the HV power supply at a level that provides the preset beam output energy. In this case, the laser gas is to be exchanged completely (i.e. New fill).

HV Mode	HV (kV)	RepRate (Hz)	Substrate Temp ($^{\circ}$ C)	Deposition Time (min)
	22	2	--	6
	30	5	--	6
	20	4	--	10
	20	8	500	10
	20	8	500	20
	20	8	500	30
EGY Mode	EGY (mJ)	RepRate (Hz)	Substrate Temp ($^{\circ}$ C)	Deposition Time (min)
	165	8	500*	6
	165	8	500	6
	165	8	500	10
	165	8	500	20
	165	8	500	30

Table 5.1: Observation table of the PLD parameters studied for the optimization. The shaded region of the table: deposition with no substrate heating. *Air annealed sample.

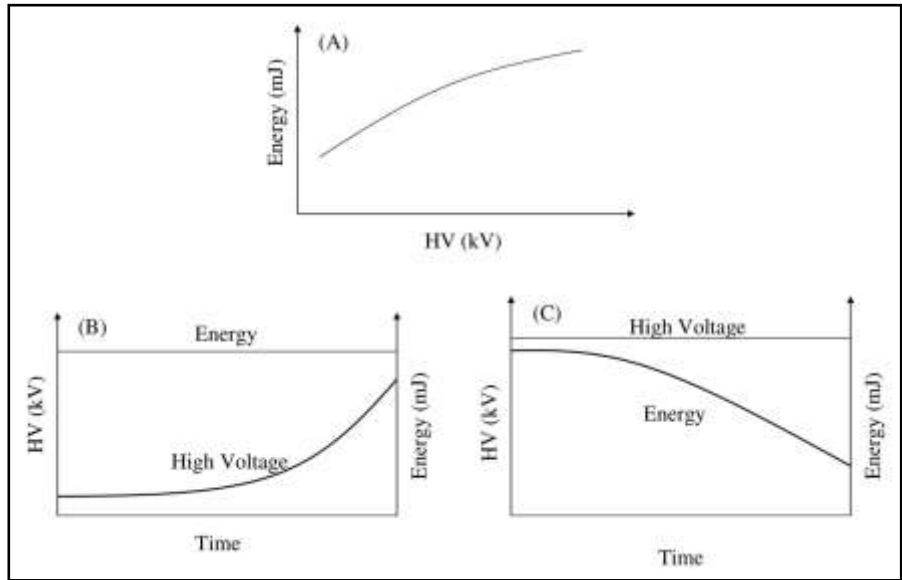


Fig. 5.1: A) Variation of energy with charging voltage. B) Constant energy mode: voltage increases with time. C) Constant voltage mode: energy decreases with time.⁴⁶

5.1.3 Parameters

Sr. No.	Parameter	Details
1.	Target	TiO ₂ (P25)
2.	Substrate	Soda Lime Glass Slide
3.	Target-Substrate Distance	38 mm
4.	Pulse Repetition Rate	8 Hz
5.	Energy	165 mJ
6.	Substrate Temperature	500 °C

Table 5.2: Parameters of PLD

5.1.4 XRD

The XRD pattern of commercial TiO₂ as shown in Fig.5.1 revealed well-defined reflections at 2θ values of 25.28°, 37.80°, 48.05°, 54.06°, 62.69°, 68.76°, 70.31° and 75.03° which are the typical characteristic peaks of Anatase TiO₂. The existence of a weak peak at about $2\theta = 30^\circ$ points out an exceptionally small amount of the brookite phase, while the rutile phase was not observed. The Fig.5.3 shows the XRD pattern of air and vacuum annealed thin films at different grazing incidence angles. The amorphous pattern reveals that the film thickness is so less that the x-rays penetrate into the substrate (glass) which is amorphous.

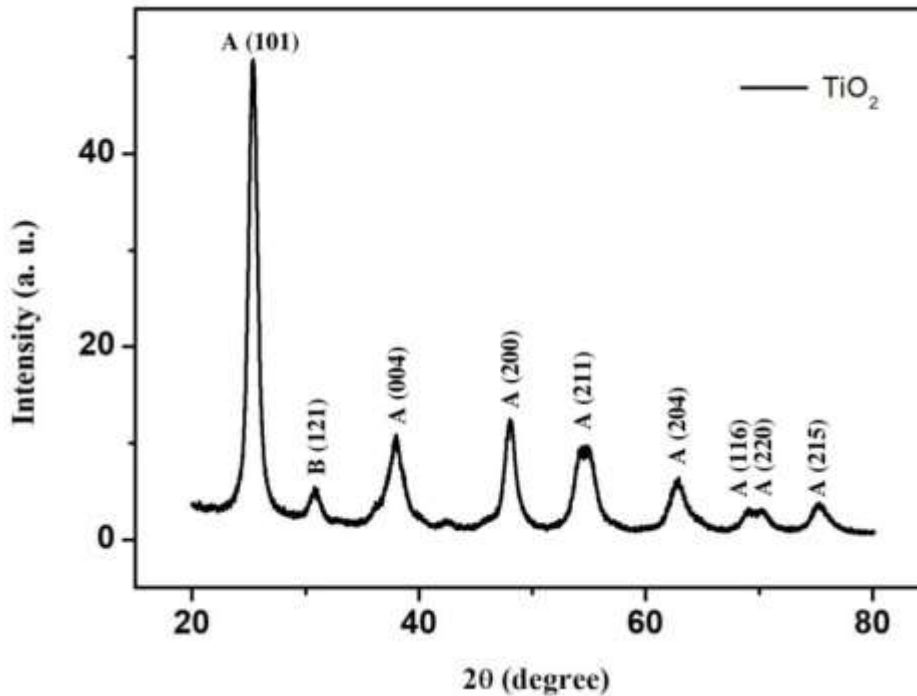


Fig. 5.2: XRD pattern of TiO₂.

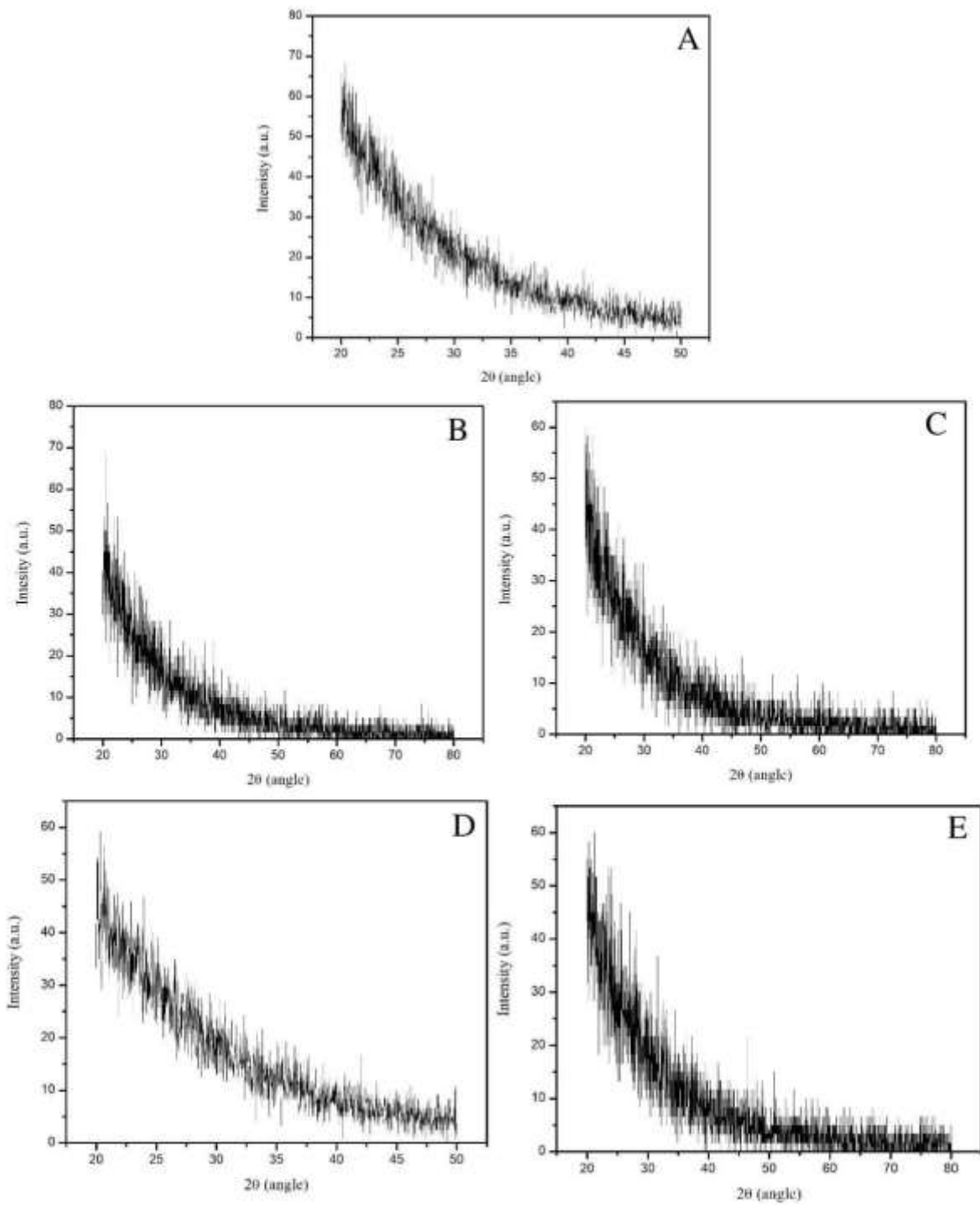


Fig. 5.3: XRD pattern of: A) Glass, B) and C) air annealed samples (at grazing incidence 1 and 0.05), D) and E) vacuum annealed sample (at grazing incidence 3 and 0.1 respectively).

5.1.5 FTIR

The FT-IR spectrum of TiO₂ showed various characteristic peaks as shown in Fig. 5.4. In this spectrum, the intensive and broad band at low wavenumber range between 400 and 800 cm⁻¹ were ascribed to the strong stretching vibrations of Ti–O and Ti–O–Ti bonds⁴⁹. The absorption band at 3454 cm⁻¹ is related to stretching and 1631 cm⁻¹ to bending vibration of O–H, representing the water as moisture.⁵⁰

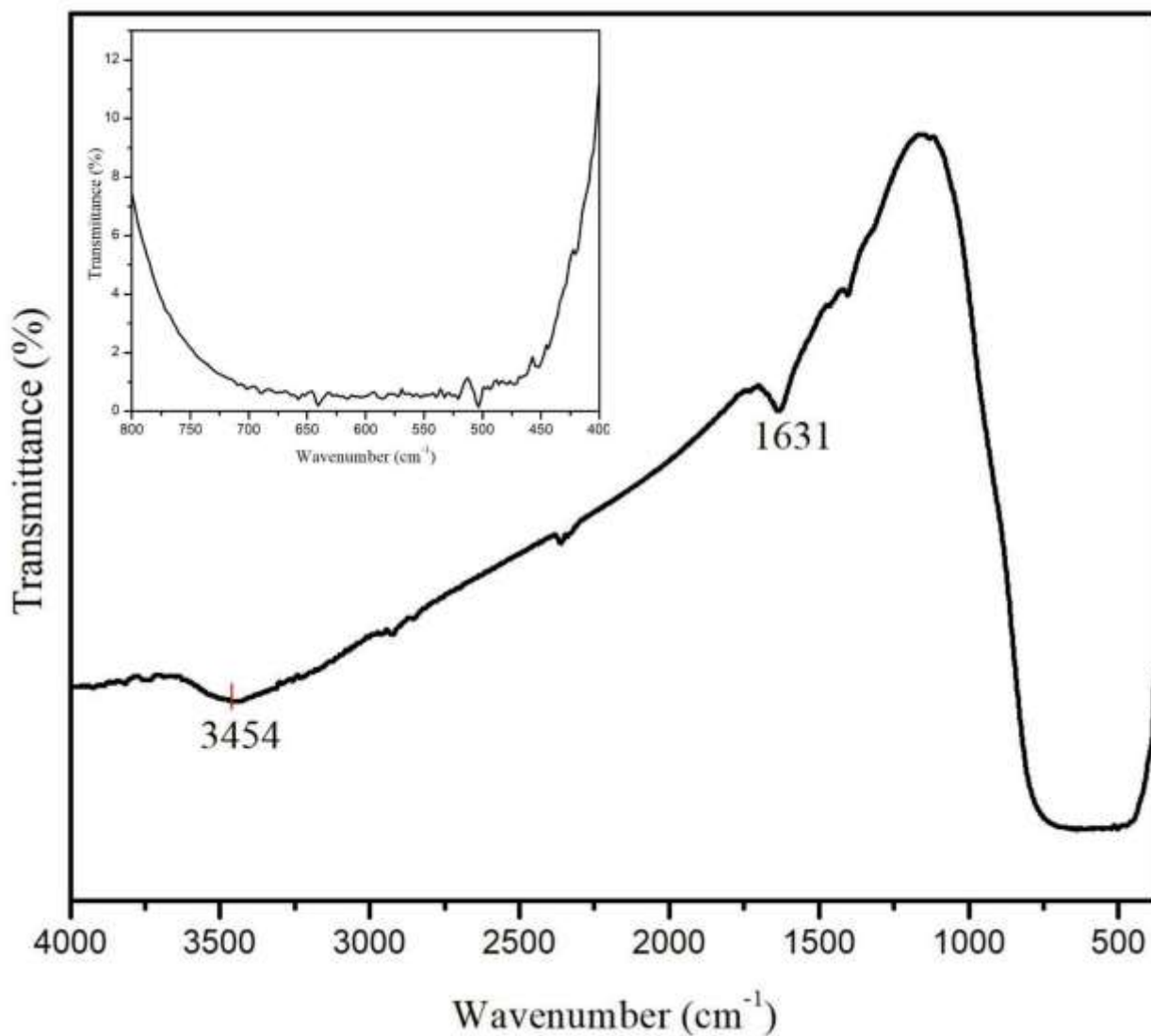


Fig. 5.4: FTIR spectrum of TiO₂

5.1.6 SEM

The SEM images of the surface morphology of the deposited thin films on the soda lime glass substrate are shown in the Fig. 5.5. From Fig. 5.5 A and B, we can see that the deposited film is not uniform across the surfaces of the substrate; the density of the deposited particles is not uniform; at some regions, the growth density is very high and at other regions it is very low. This non-uniformity results in varying thickness of the film. The non-uniformity depends on the following factors: ‘rotation of target and the substrate’ and ‘distance between the target and the substrate’. If target and the substrate are made to rotate in the opposite directions during the deposition, the deposition will be uniform. The target-substance distance should be such a way that the plume touches the entire surface of the substrate. In our case we have kept the target-substrate distance to be 38 mm.

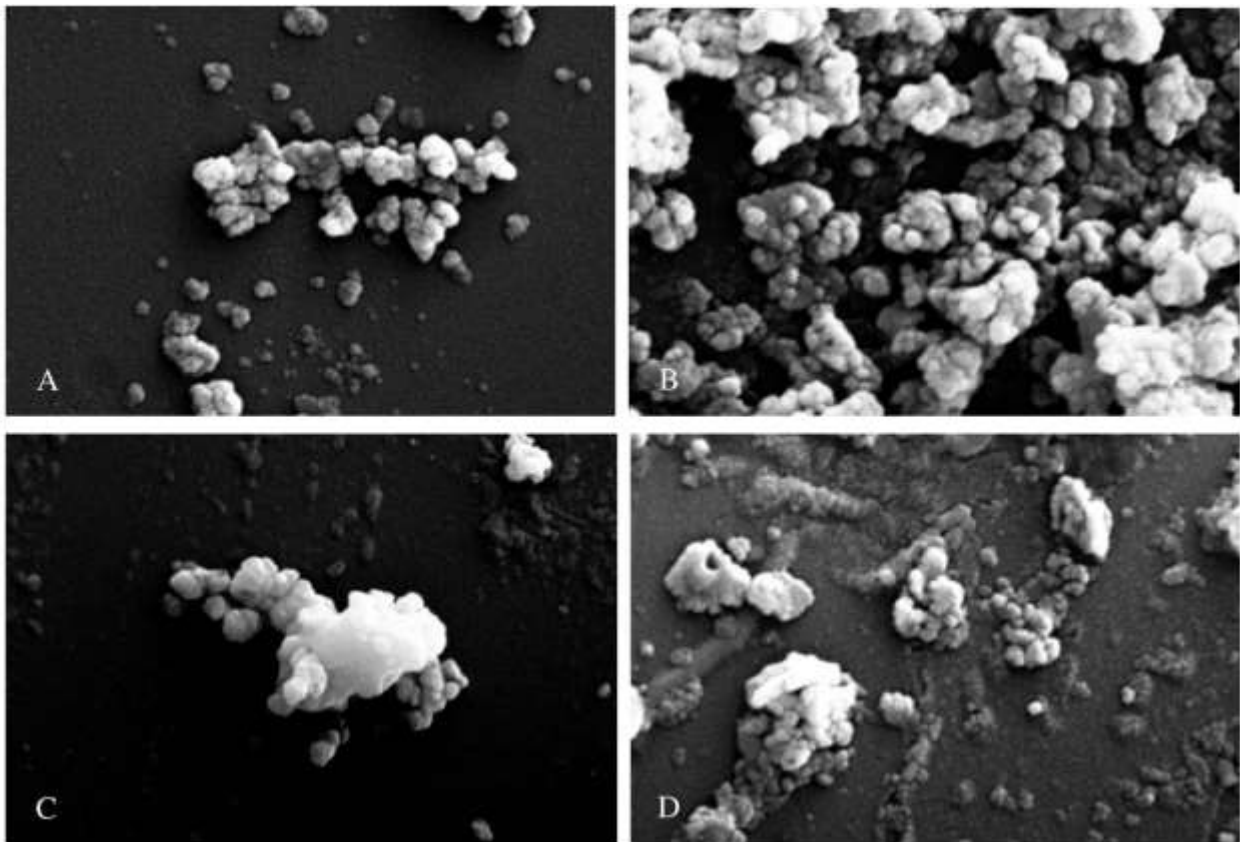


Fig. 5.5: A) Low density of Island aggregation which primarily depends on replate and laser fluence. B) High density of Island aggregation of the same sample showing uneven film deposition. C) A typical Island formation in PLD. D) Morphology of the air-annealed sample.

Effect of pulse repetition rate (replate): The density and the quality of the film can be controlled by optimizing pulse repetition rate (replate), laser fluence (or energy), and the substrate temperature. We have done series of experiments to optimize the parameters. We started with low replate, i.e. 2Hz and increased till 8 Hz which was found to be sufficient. The

pulse repetition plays an important role in controlling the density of the deposited particles. At a low pulse repetition rate, there is such a longer pulse interval that islands are given more time to ripen (Fig 5.4 A). Thus, the total of cluster (or island) density reduces and film aggregation tends to compact shape. The deposition time can effect on islands aggregation to a certain extent; a smooth surface can be obtained if deposition rates are chosen by varying the number of shots per second, keeping the amount deposited per shot constant. Thus, the laser repetition rate plays an important role in smoother films growth process. It also affects the deposition and diffusion rates if desorption and sputtering of the ablated particles are neglected.^{10, 51}

Effect of laser fluence (energy): The instantaneous flux of highly energetic depositing species is strongly dependent on the laser fluence. The number of ions deposited in the first pulse is not enough to generate stable nucleation centers, and thus non-stable centers are produced. The incoming species from the next laser pulse tend to stabilize these nucleation centers by the addition of new species. After a few pulses, a stationary regime is reached and the arriving species join the stabilized centers that become islands (Fig 5.4 C). Together with the laser repetition rate, the most direct way to increase the particle flux is to raise the laser fluence. Incoming energetic species produce the self-sputtering of a fraction of the already deposited metal. Self-sputtering yield increases with the kinetic energy and the degree of ionization of the incoming species. These two parameters are strongly correlated and increase with the laser fluence.^{10,52}

Effect of the crystallinity of the substrate: Irrespective of the deposition technique, the substrate can play an active role in the nucleation process in PLD as it is believed that a significant percentage of nucleation centers for the clusters occur at point defects, generated by the high fluxes of energetic atoms of the plume, and the nucleation rate is linear with the average flux. For crystalline substrates, a minimum requirement for the epitaxial growth to be fulfilled is that the lattice mismatch between the materials to be deposited on the substrate has to be lower than 9%. The shape of the clusters changes when crystalline substrates are used with respect to the amorphous one.¹⁰

Lattice parameter of the nanoparticulate film on glass substrate demonstrates the closest match to that of the bulk material as compared to the film on crystalline substrate. The slight deviation in the lattice parameters of thin films on the single crystal substrates from the single crystal bulk sample may be due to the substrate induced strain in the film. However, glass, being an amorphous substrate, does not provide any substrate induced strain and hence the films grow completely relaxed leading to its lattice parameter being very close to the bulk value. Usually when the lattice mismatch between the film and substrate materials is very large, the substrate control over the film growth is weak.⁵³

Effect of substrate temperature: Substrate temperature is also an important factor that affects morphology, crystallinity, and composition of the deposited material. It helps in dewetting process of thin films. The dewetting process is characterized by the breaking up of a continuous

liquid film into holes, followed by hole growth, coalescence, and finally decay into nanostructures on the substrate. This is important because the production of large supported NPs by PLD at room temperature is limited by the critical film thickness, a common method to overcome this limit and to produce surface covered with large NPs is the thermal annealing after the deposition of the film. The temperature for the dewetting to occur can be well below the melting temperature of the bulk material, and it decreases with the film thickness. The film surface exhibits a certain degree of roughness and increases as the annealing temperature increases. The surface roughness changes the optical properties of the film. The experimental conditions for annealing also effects the film properties. The air-annealed films (Fig. 5.5 D) show good crystalline order with few defects. Conversely, the vacuum-annealed films (Fig. 5.5 B) exhibit a highly disordered surface.^{10,54-56}

5.1.7 Optical properties

The TiO₂ thin films exhibit good transmission in the spectral range of 360–800 nm wavelengths. It is found that average transmittance of as-deposited and annealed TiO₂ films is about 67% in the visible region with respect to reference blank glass substrate. However, there is strong absorption in the ultraviolet region which is characterized by a sharp drop in optical transmittance. This can be ascribed to fundamental absorption of TiO₂ nanoparticulate thin film layer owing to the transition of electrons from the valence to conduction bands.

The transmittance-absorption edge for as-deposited thin film is found to be at 402 nm and for the air and vacuum annealed films the band edge is found to be at 360 nm. The transmittance absorption edge is sensitive to change in substrate temperature, which is shifted to long ultraviolet region as the substrate temperature increases.

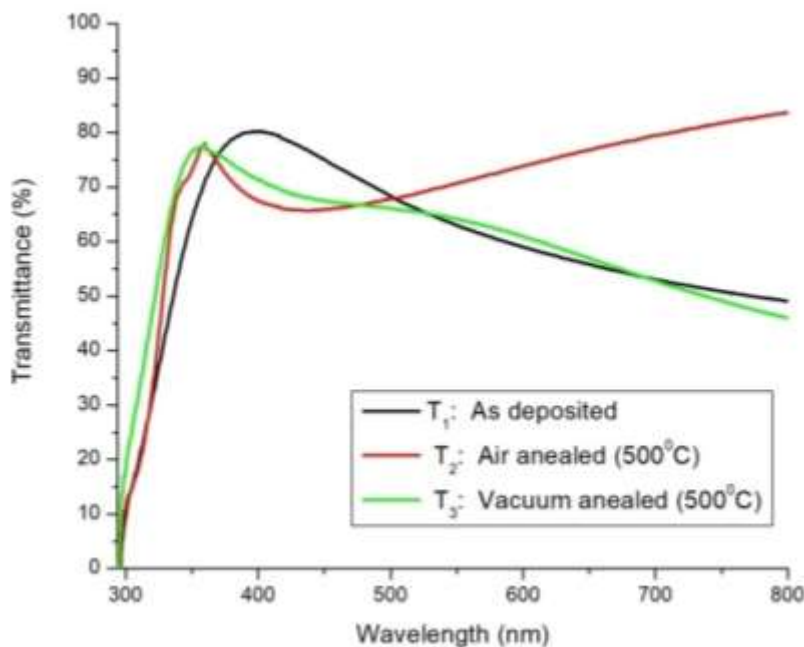


Fig. 5.6: UV-Vis spectrum of as-deposited and air and vacuum annealed thin films.

5.2 Anodization

5.2.1 Apparatus

The electrochemical setup basically comprises of a beaker containing an electrolyte, two plates; anode and cathode, power supply and a digital multimeter for current measurement. Low temperature experiment additionally includes a circulating chiller bath and a double jacketed beaker.

5.2.2 Experimental

Materials and Methods

Titanium was used as a substrate which acts as anode on which thin film deposition takes place. Platinum was used as a cathode, made up of material which is chemically inert.

Pre-treatment of titanium plate: Prior to the experiment, the titanium foil was cut in a ratio of 3.7:1.7 and mechanically polished by ultrasonicing in DI H₂O, Acetone and Isopropyl alcohol for 30 minutes each to remove the grease, debris or any sharp edges remnant on the surface of Titanium plates. The plates were then rinsed with deionised water and dried in air.

Anodization was performed using titanium plate as the working electrode and platinum as the counter electrode at room temperature and at low temperatures.

Preparation of Electrolyte

The requirement for electrolyte preparation was 0.5 wt. % of NH₄F, 2 wt. % Deionized water (DI H₂O), and 98 wt. % of Ethylene glycol (EG)⁵¹. 0.75mg NH₄F was weighed and put into a clean beaker, further adding 2.5mL DI H₂O and 147mL EG to it. The mixture was ultrasonicated for 30 minutes and then kept for ageing for approximately 72 hours. The prepared electrolyte could be stored in a desiccator for further usage.

Procedure

The Experiment consists of two sets: 1) One step anodization 2) Two step anodization and is performed in two temperature range: Room temperature and at Low temperatures.

Room temperature

Make the appropriate connections: Cathode- platinum plate, Anode- titanium plate, a power supply and a digital multimeter. Fill the beaker with prepared electrolyte up to a level such that

both the plates are halfway immersed into it completing the conductive circuit. Immerse the titanium plate as per desired surface area needed to be coated. Note down the Temperature and set the required voltage on the power supply. The experiment was carried out at potentiostatic mode (40V) by anodizing each Titanium plate at different time intervals T(s) and simultaneously noting down the values of current (mA) followed by plotting a graph of Current Density (j) v/s Time (s). Similar procedure was followed for 2nd step anodization for different time intervals. Before proceeding with the second step anodization the removal of top layer of anodised plates was done using scotch tape.

Low temperatures experiment

Low temperature was attained by using a refrigerated circulating chiller bath and the same experiment (room temperature) was performed. A circulating chiller bath is designed to maintain a low temperature which can be set manually. Inside it there is a chamber in which coolant is stored. A thermocouple (rod like structure) is dipped inside this coolant bath which controls the temperature. A double jacketed beaker was connected to the chiller by a silicon pipe through which the coolant circulated maintaining a lower temperature. Coolant was prepared by mixing 7.5L of deionised water with 4L of ethylene glycol.

The electrolyte was poured in the double jacketed beaker making all the necessary connections and setting the temperature on the circulating chiller bath to carry out the experiments.

5.2.3 Observations

SET-1

Temperature (°C)	Time (s)
1st step anodization	
12.5	30
2.2	120
2nd step anodization	
0.9	120
0.5	300

SET-2

Temperature (°C)	Time (s)
1st step anodization	
4.8	20
4.1	25
4.0	30
2nd step anodization	
3.8	60
3.3	300
3.2	600

5.2.4 SEM

SET-1

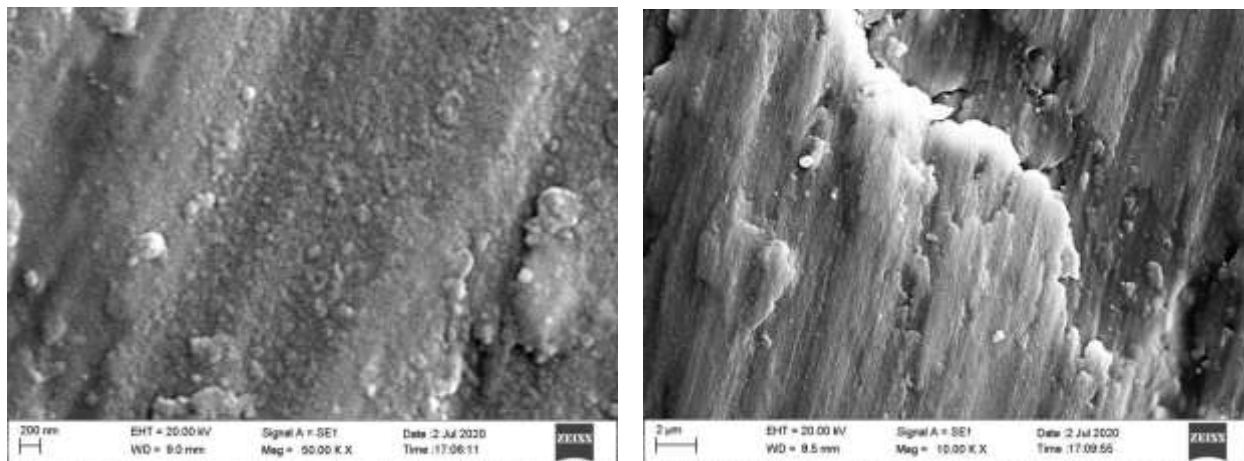


Fig. 5.6: SEM images of anodized plates(Set-1)

Growth of thick oxide barrier layer on the surface of titanium is observed.

SET-2

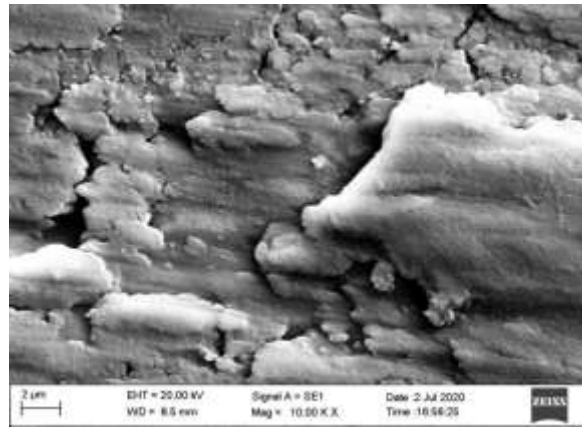
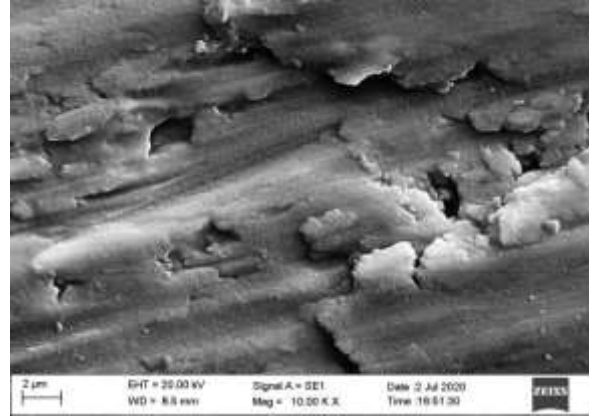
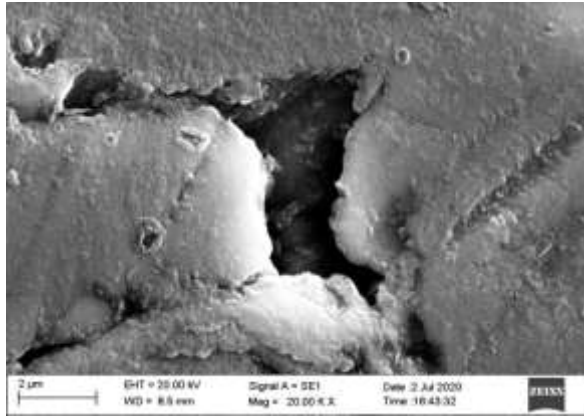


Fig. 5.7: SEM images of anodized plates (Set-2)

Conclusions

Different parameters of pulsed laser deposition are being studied and optimized. The deposited films with optimized parameters were studied using Scanning Electron Microscopy (SEM) and UV-Visible Spectroscopy. UV visible transmission is studied to understand the transmission properties and band edge positions of the as-deposited and annealed TiO₂ films. SEM images reveal effect of variation of different parameters on the film morphology as inferred from the literature report. Nature of the bulk TiO₂ is being studied using X-Ray Diffraction (XRD) and Fourier Transform Infra-Red (FTIR) Spectroscopy. From XRD studies the bulk TiO₂ was found to be in anatase phase with small amount of brookite phase. FTIR studies also reveal the purity of TiO₂ with only water as moisture. The XRD studies for the deposited films show the thickness of the films to be very less.

The anodized samples are amorphous in nature and heat-treated at 500°C for 1 hour to form crystalline phases (anatase, rutile etc.). UV visible absorption is studied to understand the band edge position of TiO₂ nanotubes with respect to change in wall thickness as well as the thickness of these TiO₂ thin film samples. FTIR studies were done to find any remnant fluorine and carbon, present on the surface of TiO₂ nanotubes due to adsorbed molecules from anodization bath, having NH₄F and ethylene glycol. Surface morphology was studied using SEM and found to be nanotubes covered with thick layer of nanoparticles on the top converting the entire nanotubular structures.

References

- [1] Infrared spectroscopy studies of adsorption and photochemistry on TiO₂ surfaces- Andreas Mattson.
- [2] Recent advances in syntheses, properties and applications of TiO₂ nanostructures by Imran Ali, ^{*ab}MohdSuhail, ^bZeid A. Allothman^c and Abdulrahman Alwarthan^c. DOI: 10.1039/c8ra06517.
- [3] Nanostructures and nanomaterials: Synthesis, Properties and Applications. – Guozhong Cao.
- [4] Eason, R., 2006. *Pulsed Laser Deposition of Thin Films*. 1st ed. New Jersey and Canada: John Wiley & Sons, Inc., Hoboken.
- [5] Miller, J., 1994. *Laser Ablation, principles and applications*. 1st ed. Berlin Heidelberg New York: Springer-Verlag.
- [6] Stafe, M., Marcu, A. and N. Puscas, N., 2014. *Pulsed Laser Ablation of Solids, Basics, Theory and Applications*. 1st ed. Heidelberg New York Dordrecht London: Springer-Verlag.
- [7] J.R, H., et al, 1995. Computational study of heat transfer and gas dynamics in the pulsed laser evaporation of metals. *Journal of Applied Physics*, 78, 3.
- [8] H. A. Lutey, A., 2013. An improved model for nanosecond pulsed laser ablation of metals. *Journal of Applied Physics*, 114, 1-11.
- [9] Li, G., 2008. Role of pulse repetition rate in film growth of pulsed laser deposition. *Science Direct*, 266, 1-5.
- [10] Ion N, M. and Anna Paola, C., 2018. *Pulsed Laser Ablation, Advances and Applications in Nanoparticles and Nanostructuring Thin Films*. 1st ed. Penthouse Level, Suntec Tower 3 8 Temasek Boulevard Singapore: Pan Stanford Publishing Pte. Ltd..
- [11] Hasan, M. , Haseeb, A. , Saidur, R. , Masjuki, H. (2008), 'Effects of Annealing Treatment on Optical Properties of Anatase TiO₂ Thin Films', World Academy of Science, Engineering and Technology, Open Science Index 16, International Journal of Mechanical and Mechatronics Engineering, 2(4), 410 - 414.
- [12] A. Sambri et al, 2007. Substrate heating effects on the propagation dynamics of laser produced plume during pulsed laser deposition of oxides Applied Surface Science 254 , 790–793
- [13] R. Fu-Xio, 1995. Liquid target pulsed laser deposition. Appl. Phys. Lett. **67**, 1022.
- [14] R. Delmdahl et al, 2008. “Pulsed laser deposition with excimer lasers”. Phys. stat. sol. (c) 5, No. 10, 3276–3279.

- [15] R.F. Wood et al, 1998. Dynamics of plume propagation, splitting, and nanoparticle formation during pulsed-laser ablation. *Applied Surface Science* 127–129, 151–158.
- [16] D.B. Geohegan, “Diagnostics and characteristics of pulsed laser deposition laser plasmas”, in ref. 3, pp.115-165.
- [17] J.S. Horwitz and J.A. Sprague, “Film nucleation and film growth in pulsed laser deposition of ceramics”, in ref. 3, pp.229-254.
- [18] S. Metev, “Process characteristics and film properties in pulsed laser deposition”, in ref.3, pp.255-264.
- [19] J. A. Michael, 2008. “Film growth mechanisms in pulsed laser deposition”. *ApplPhysA* 93: 579–587
- [20] Intechopen. 2016. Laser-Induced Plasma and its Applications. [ONLINE] Available at: <https://www.intechopen.com/books/plasma-science-and-technology-progress-in-physical-states-and-chemical-reactions/laser-induced-plasma-and-its-applications>. [Accessed 3 June 2020].
- [21] A. E. Seigman, 1986. *Lasers*. 1st ed. Mill Valley, California: University Science Books.
- [22] W. Stephan and G. Christoph, 2018. “[Lasers in Medical Diagnosis and Therapy](#).” IOP Publishing Ltd, 1-36.
- [23] Eichhorn, M., 2014. *"Laser Physics"*. 1st ed. Cham Heidelberg New York Dordrecht London: Springer.
- [24] E.L, Saldin, E.A, Schneidmiller. and M.V, Yurkov, 2000. *"The Physics of Free Electron Lasers"*. 1st ed. Berlin Heidelberg New York: Springer-Verlag.
- [25] Raymond, C., 1990. *"X Ray Lasers"*. 1st ed. Boston, San Diego, New York: Academic Press Inc..
- [26] Lucien, D., 1994. *"Excimer Lasers"*. 1st ed. Berlin Heidelberg, New York, London: Springer-Verlag.
- [27] Basting, D. and Marowsky, M., 2005. *"Excimer Laser Technology"*. 1st ed. Berlin Heidelberg: Springer-Verlag.
- [28] Rhodes, C., 1984. *"Excimer Lasers"*. 1st ed. Berlin Heidelberg, New York: Springer-Verlag.
- [29] W.L. Morgan and A. Szoke, 1981. “Kinetic processes in Ar-Kr-F₂ laser mixtures.” *PhysRevA*.23.1256
- [30] N. G. Basov et al, 1984. “Electron-beam-controlled atomic Xe infrared laser.” *Soviet Journal of Quantum Electronics*.14.9

- [31] American Institute of Physics. 2006. AVS Reference Guide-Glossary. [ONLINE] Available at: <https://web.archive.org/web/20060304160701/http://www.aip.org/avsguide/refguide/glossary.html>. [Accessed 1 May 2020].
- [32] M. Hoffmann, D., H. Thomas, J. and Singh, B., 1997. *"Handbook of Vacuum Science and Technology"*. 1st ed. New York: Elsevier Science & technology Books.
- [33] V. Staurt, R., 1983. *"Vacuum Technology, Thin Films and Sputtering"*. 1st ed. New York: ACADEMIC PRESS INC..
- [34] Pfeiffer Vacuum. 2020. HiPace 300. [ONLINE] Available at: <https://www.pfeiffer-vacuum.com/en/products/vacuum-generation/turbopumps/hybrid-bearing/hipace-300/5025/hipace-300-for-tcp-350-dn-100-iso-k>. [Accessed 5 June 2020].
- [35] ExportersIndia. 2020. Rotary Vacuum Pump. [ONLINE] Available at: <https://www.exportersindia.com/melkev-machinery-impex-company5417353/rotary-vacuum-pump-3535175.htm>. [Accessed 5 June 2020].
- [36] sens4. 2020. Pirani-Working-Principle. [ONLINE] Available at: <https://sens4.com/pirani-working-principle.html>. [Accessed 24 June 2020].
- [37] hakuto-vacuum. 2020. Pfeiffer_Vacuum. [ONLINE] Available at: http://www.hakuto-vacuum.jp/pfeiffer_vacuum/pdf/Gauge/TPR280.pdf. [Accessed 24 June 2020].
- [38] Idealvac. 2020. Pfeiffer IKR 251 Cold Cathode Vacuum Gauge Transmitter. [ONLINE] Available at: <https://www.idealvac.com/Pfeiffer-IKR-251-Cold-Cathode-Vacuum-Gauge-Transmitter/pp/P109334>. [Accessed 24 June 2020].
- [39] TiO₂ Nanotubes: Synthesis and Applications Poulomi Roy, Steffen Berger, and PatrikSchmuki* DOI: 10.1002/anie.201001374
- [40] Catalyst-Doped Anodic TiO₂ Nanotubes: Binder-Free Electrodes for (Photo)Electrochemical Reactions by Hyeonseok Yoo, Moon-su Kim, Yong-Tae Kim, Kiyong Lee and Jinsub Choi. doi.org/10.3390/catal8110555
- [41] TiO₂ Nanotubes: Self-organised electrochemical formation, properties and applications by J.M Macak, H.Tsuchiya, A. Ghicov, K. Yasuda, R. Hahn, S. Bauer, P. Schmuk* .
- [42] A Review on the Electrochemically Selforganized Titania Nanotube Arrays: Synthesis, Modifications, and Biomedical Applications by Yu Fu and Anchun Mo*
- [43] A Review on TiO₂ Nanotubes: Influence of Anodization Parameters, Formation Mechanism, Properties, Corrosion Behavior, and Biomedical Applications by K. Indira^{1,3} et. Al

- [44] Gems-Inclusions. 2020. FTIR Spectroscopy. [ONLINE] Available at: <https://www.gems-inclusions.com/inclusions-studies/analytical-methods/ftir-spectroscopy/>. [Accessed 9 June 2020].
- [45] S. R. Fellipsy et al, 2018. Experimental methods in chemical engineering: Ultraviolet visible spectroscopy—UV-Vis. *The Canadian Journal of Chemical Engineering*, 96, 2512-2517.
- [46] Manualzz. 2020. USER MANUAL COMPexPro™ Series 10/2005. [ONLINE] Available at: <https://manualzz.com/doc/4206242/user-manual-compexpro%E2%84%A2-series-10-2005>. [Accessed 9 May 2020].
- [47] Baskaran, Sulochanadevi. (2010). Structure and Regulation of Yeast Glycogen Synthase. https://www.researchgate.net/publication/47418334_Structure_and_Regulation_of_Yeast_Glycogen_Synthase
- [48] Raza, Mohsin. (2012). Synthesis of hydrogenated amorphous carbon (a-C:H) thin films by HiPIMS-based processes. 10.13140/RG.2.1.2971.0242.
- [49] C. Xiuwen et al, 2016. *Arabian Journal of Chemistry*: 9, S1706–S1711
- [50] S.W. Hwang et al, 2014. *Sensor Letters* 12, 1–5. DOI: 10.1166/sl.2014.3224
- [51] Li G. et al, 2008. “Role of pulse repetition rate in film growth of pulsed laser deposition.” *Nuclear Instruments and Methods in Physics Research*, B 266, 57-62
- [52] Ohnishi, T., 2005. Improved stoichiometry and misfit control in perovskite thin film formation at a critical fluence by pulsed laser deposition. *Applied Physics Letters*, 87, 241919
- [53] Tiwari S. et al, 2007. *J. Phys. D: Appl. Phys.* **40**, 4943–4947
- [54] W. Yang et al, 2006. “An investigation of annealing on the dielectric performance of TiO₂ thin films”. *Semicond. Sci. Technol.* **21**: 1573–1579
- [55] C. Sudakar et al, 2008. “Room temperature ferromagnetism in vacuum-annealed TiO₂ thin films”. *Journal of Magnetism and Magnetic Materials* 320: L31-L36
- [56] M. M. Hasan et al, 2008. “Effects of Annealing Treatment on Optical Properties of Anatase TiO₂ Thin Films.” *World Academy of Science, Engineering and Technology* **16**: 04-20